

Robust Constrained Hyperspectral Unmixing Using Reconstructed-Image Regularization

Kazuki Naganuma, *Student Member, IEEE*, Yuki Nagamatsu, Shunsuke Ono, *Member, IEEE*,

Abstract—Hyperspectral (HS) unmixing is the process of decomposing an HS image into material-specific spectra (endmembers) and their spatial distributions (abundance maps). Existing unmixing methods have two limitations with respect to noise robustness. First, if the input HS image is highly noisy, even if the balance between sparse and piecewise-smooth regularizations for abundance maps is carefully adjusted, noise may remain in the estimated abundance maps or undesirable artifacts may appear. Second, existing methods do not explicitly account for the effects of stripe noise, which is common in HS measurements, in their formulations, resulting in significant degradation of unmixing performance when such noise is present in the input HS image. To overcome these limitations, we propose a new robust hyperspectral unmixing method based on constrained convex optimization. Our method employs, in addition to the two regularizations for the abundance maps, regularizations for the HS image reconstructed by mixing the estimated abundance maps and endmembers. This strategy makes the unmixing process much more robust in highly-noisy scenarios, under the assumption that the abundance maps used to reconstruct the HS image with desirable spatio-spectral structure are also expected to have desirable properties. Furthermore, our method is designed to accommodate a wider variety of noise including stripe noise. To solve the formulated optimization problem, we develop an efficient algorithm based on a preconditioned primal-dual splitting method, which can automatically determine appropriate stepsizes based on the problem structure. Experiments on synthetic and real HS images demonstrate the advantages of our method over existing methods.

Index Terms—Hyperspectral unmixing, mixed noise, primal-dual splitting, stripe noise, constrained optimization

I. INTRODUCTION

HYPERSPECTRAL (HS) images are three-dimensional cube data consisting of two-dimensional spatial information and one-dimensional spectral information. Compared to grayscale or RGB images, HS images provide more than several hundred bands, each of which contains specific unique wavelength characteristics of materials such as minerals, soils, and liquids. Therefore, HS images have various applications, such as ecology, mineralogy, biotechnology, and agriculture

[1]–[4]. Due to the trade-off between spatial resolution and spectral resolution, HS sensors do not have a sufficient spatial resolution, resulting in containing multiple components (called endmembers) in a pixel [5], which refers to as a mixel. The process of decomposing the mixel into endmembers and their abundance maps is called unmixing. Unmixing has been actively studied in the remote sensing field because it is essential for the analysis of HS images [6], [7]. It is also used for denoising [8], [9], data fusion [10], [11], and other related applications.

Unmixing methods fall into two categories according to their assumptions: non-blind and blind unmixing. Non-blind unmixing methods estimate abundance maps from a given endmember library. Endmembers in the library are potentially much larger in number than endmembers included in real HS images, i.e., its corresponding abundance maps become sparse. Thus, sparse regression-based methods have been proposed for non-blind unmixing [12]–[21]. On the other hand, blind unmixing methods simultaneously estimate an endmember library and abundance maps, allowing us to obtain the abundances of endmembers whose spectral libraries are unknown. For blind unmixing, learning-based methods have attracted attention [22]–[24]. Learning-based methods often involve the following steps: extraction of initial endmembers from an input HS image, estimation of corresponding initial abundance maps by some non-blind unmixing methods, and then learning of sophisticated unmixing and reconstruction networks based on this information. Therefore, non-blind unmixing is a fundamental task that must precede blind unmixing. Henceforth, non-blind unmixing will simply be referred to as unmixing.

Most existing unmixing methods have adopted a linear mixing model (LMM) due to its simplicity and efficiency [25], [26]. In the LMM, an HS image is represented by a linear combination of the endmembers and their corresponding abundance maps. Since non-blind unmixing assumes that the endmember library is given, the abundance maps can be easily estimated from noiseless HS images by solving linear equations. However, observed HS images are often contaminated by various types of noise, such as random noise, outliers, missing values, and stripe noise, due to environmental and sensor issues. Since these types of noise affect the unmixing performance, it is essential to establish unmixing techniques robust to such noises.

Many noise-robust unmixing techniques explicitly model noises and then take the approach of solving optimization problems that incorporate functions characterizing abundance maps [12]–[21]. The methods in [12], [14], [19]–[21] employ a sparse regularization, which is based on the fact that HS

Manuscript received XXX, XXX; revised XXX XXX, XXX.

K. Naganuma is with the Department of Computer Science, Tokyo Institute of Technology, Yokohama, 226-8503, Japan (e-mail: naganuma.k.aa@m.titech.ac.jp).

Y. Nagamatsu is with the Department of Computer Science, Tokyo Institute of Technology, Yokohama, 226-8503, Japan.

S. Ono is with the Department of Computer Science, Tokyo Institute of Technology, Yokohama, 226-8503, Japan (e-mail: ono@c.titech.ac.jp).

This work was supported JST, the establishment of university fellowships towards the creation of science technology innovation, under Grant JPMJFS2112, in part by JST PRESTO under Grant JPMJPR21C4, and in part by JSPS KAKENHI under Grant 22H03610, 22H00512, 20H02145, and 18H05413.

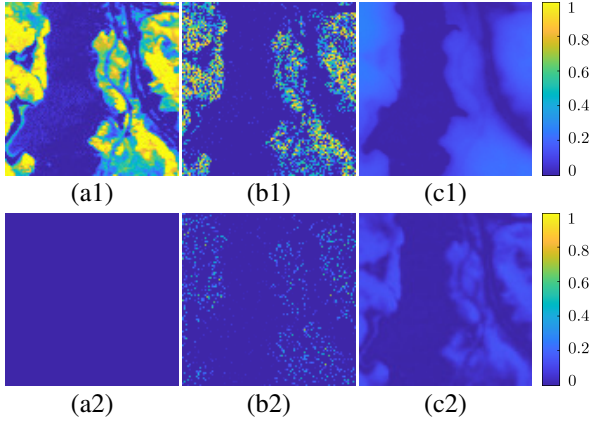


Fig. 1. Unmixing results of JSTV [15]. The first row shows the abundance map whose corresponding endmember exist in an HS images. The second row shows the abundance map whose corresponding endmember does not exist in an HS image. (a): Original abundance maps. (b): Estimated abundance maps when the weight of sparsity regularization is increased. (c): Estimated abundance maps when the weight of smoothness regularization is increased.

images consist of a small fraction of the endmembers in a library and is the basis of sparse regression-based methods. In addition, the methods in [13], [15]–[18] adopt a combination of sparse and piecewise-smooth regularizations. In general, abundance maps are piecewise smooth because neighboring pixels often have the same endmember. We will give detailed reviews of these related works in Sec. III.

A. Motivations and Contributions

As we have discussed, various studies have been carried out to mitigate the effects of noise in unmixing, but there are still two limitations in terms of robustness to noise. The first is that the performance of unmixing is severely degraded when the input HS image is contaminated with high levels of noise. The second is that existing unmixing methods cannot adequately deal with stripe noise.

As reviewed in the previous subsection, many existing unmixing methods use a combination of sparse and piecewise-smooth regularization to characterize the abundance maps. However, as shown in Fig. 1, balancing these regularizations becomes very difficult when unmixing HS images contaminated with high levels of noise. In fact, if the weight of the sparse regularization is increased, a large amount of noise remains in the estimated abundance maps. Conversely, if the weight of the piecewise-smooth regularization is increased, the estimated abundance maps will contain many inappropriate components that are not present in the original HS image. In existing methods, adjusting the weights to avoid both problems is a very sensitive and tedious task.

To resolve this difficulty, we focus on the regularizations for the HS image reconstructed by mixing the estimated abundance maps and the endmembers, in addition to the regularizations for the abundance maps. Our assumption is the following: if the reconstructed HS image has desirable properties in its spatio-spectral structure, then the estimated abundance maps used for reconstruction should also have desirable properties. Therefore, we believe that incorporating

spatio-spectral regularization for HS images into the unmixing formulation can improve the unmixing performance in high-noise situations where abundance maps are difficult to estimate using existing methods.

Regarding the second limitation, existing unmixing methods mainly deal with Gaussian noise and sparse noise. However, in addition to these noises, actual HS images are often contaminated with stripe noise, mainly due to external disturbances and calibration errors [27]–[29]. Since stripe noise is non-Gaussian and non-sparse, it cannot be handled by existing methods, leading to performance degradation in unmixing.

Based on the above discussion, we propose a new robust constrained hyperspectral unmixing method based on convex optimization (RCHU). In terms of the features of RCHU, the contributions of the paper can be summarized as follows.

- (*Robust to high levels of noise*): RCHU employs not only the abundance map regularizations but also the regularizations for the reconstructed HS image (called reconstructed-image regularizations). In the context of HS image restoration, many effective HS image regularizations have been studied [30]–[36]. By incorporating them as reconstructed-image regularizations, we can robustify the unmixing process under highly-noisy scenarios.
- (*Robust to mixed noise including stripe noise*): By explicitly modeling three types of noise (Gaussian-like random noise, sparse noise, and stripe noise), RCHU can adequately handle mixed noise, including stripe noise, which is difficult to handle in existing methods.
- (*Easy to adjust hyperparameters*): We formulate the unmixing problem as a constrained convex optimization problem, where we model data-fidelity and noise terms as hard constraints instead of adding them to the objective function. This type of constrained formulation decouples interdependent hyperparameters into independent ones, thus facilitating parameter settings, which will be detailed in Sec. IV-A.
- (*Eliminating the need to adjust stepsizes*): In order to solve our optimization problem for unmixing, we develop an efficient algorithm based on the preconditioned primal-dual splitting method (P-PDS) [37] with an operator-norm-based stepsize selection method [38], [39]. Unlike the standard PDS [40], the P-PDS can automatically determine the appropriate stepsizes based on the problem structure. Unlike the optimization algorithms used in existing unmixing methods, our P-PDS-based algorithm can automatically determine the appropriate stepsizes based on the problem structure.

Experiments on synthetic and real HS images demonstrate the advantages of RCHU over existing methods.

B. Organization

The paper is organized as follows. In Section II, we introduce the mathematical tools. In Section III, we briefly review several existing unmixing methods related to our work. In Section IV, we explain the proposed method, RCHU, with its formulation and algorithm. In Section V, we conduct experiments to show the superiority of RCHU over the existing methods. Finally, we conclude the paper in Section VI.

II. PRELIMINARIES

A. Notation

In this paper, we denote the sets of real numbers and non-negative real numbers as \mathbb{R} and \mathbb{R}_+ , respectively. Matrices are denoted by capitalized boldface letters (e.g., \mathbf{X}), and the element in the i th row, j th column of matrix \mathbf{X} is denoted by $\mathbf{X}_{i,j}$. The HS image with the number of bands l and spatial size $n = n_1 \times n_2$ is treated as a matrix of size $l \times n$ and $[\mathbf{X}]_{(i,j,k)}$ indicates that the (i, j, k) th value of the cube data. The ℓ_1 -norm $\|\cdot\|_1$, the Frobenius norm $\|\cdot\|_F$, the mixed $\ell_{1,2}$ -norm grouped by row $\|\cdot\|_{1,2,r}$, and the mixed $\ell_{1,2}$ -norm grouped by column $\|\cdot\|_{1,2,c}$ are defined by $\|\mathbf{X}\|_1 = \sum_{i,j} |\mathbf{X}_{i,j}|$, $\|\mathbf{X}\|_F = \sqrt{\sum_{i,j} \mathbf{X}_{i,j}^2}$, $\|\mathbf{X}\|_{1,2,r} = \sum_i \sqrt{\sum_j \mathbf{X}_{i,j}^2}$, and $\|\mathbf{X}\|_{1,2,c} = \sum_j \sqrt{\sum_i \mathbf{X}_{i,j}^2}$, respectively. Let $\mathbf{G} \in \mathbb{R}^{M_1 \times N_1} \rightarrow \mathbb{R}^{M_2 \times N_2}$ be a linear operator. A linear operator \mathbf{G}^* is called the adjoint operator of \mathbf{G} if it is satisfied with $\langle \mathbf{G}(\mathbf{X}), \mathbf{Y} \rangle = \langle \mathbf{X}, \mathbf{G}^*(\mathbf{Y}) \rangle$ for any $\mathbf{X} \in \mathbb{R}^{M_1 \times N_1}$ and $\mathbf{Y} \in \mathbb{R}^{M_2 \times N_2}$.

B. Proximal Tools

Let f be a lower semi-continuous proper convex function on $\mathbb{R}^{M \times N}$. If $C \subset \mathbb{R}^{M \times N}$ satisfies $\lambda \mathbf{X} + (1 - \lambda) \mathbf{Y} \in C$ for any $\mathbf{X}, \mathbf{Y} \in C$ and $\lambda \in [0, 1]$, C is a convex set. For a non-empty closed convex set C , the indicator function $\iota_C : \mathbb{R}^{M \times N} \rightarrow (-\infty, \infty]$ is defined by

$$\iota_C(\mathbf{X}) := \begin{cases} 0, & \text{if } \mathbf{X} \in C, \\ \infty, & \text{otherwise.} \end{cases} \quad (1)$$

For any $\gamma > 0$, the proximity operator of f is defined by

$$\text{prox}_{\gamma f}(\mathbf{X}) := \underset{\mathbf{Y} \in \mathbb{R}^{M \times N}}{\text{argmin}} f(\mathbf{Y}) + \frac{1}{2\gamma} \|\mathbf{X} - \mathbf{Y}\|_F^2. \quad (2)$$

For an indicator function ι_C of a nonempty closed convex set $C \subset \mathbb{R}^{M \times N}$, its proximity operator is equivalent to the projection onto C , as given by

$$\begin{aligned} \text{prox}_{\gamma \iota_C}(\mathbf{X}) &= \underset{\mathbf{Y} \in C}{\text{argmin}} \frac{1}{2\gamma} \|\mathbf{X} - \mathbf{Y}\|_F^2 \\ &= \underset{\mathbf{Y} \in C}{\text{argmin}} \|\mathbf{X} - \mathbf{Y}\|_F. \end{aligned} \quad (3)$$

The Fenchell-Rockerfellar conjugate function f^* of the function f is defined by

$$f^*(\mathbf{Y}) := \sup_{\mathbf{X} \in \mathbb{R}^{M \times N}} \{\langle \mathbf{X}, \mathbf{Y} \rangle - f(\mathbf{X})\}. \quad (4)$$

Thanks to Moreus's identity, the proximity operator of f^* is efficiently calculated as

$$\text{prox}_{\gamma f^*}(\mathbf{X}) = \mathbf{X} - \gamma \text{prox}_{\frac{1}{\gamma} f}\left(\frac{1}{\gamma} \mathbf{X}\right). \quad (5)$$

C. Preconditioned Primal-Dual Splitting Method (P-PDS)

Let f_i ($i = 1, \dots, N$) and g_j ($j = 1, \dots, M$) be lower semi-continuous proper convex functions. Consider a convex optimization problem of the following form:

$$\begin{aligned} \min_{\substack{\mathbf{Y}_1, \dots, \mathbf{Y}_N \\ \mathbf{Z}_1, \dots, \mathbf{Z}_M}} & \sum_{i=1}^N f_i(\mathbf{Y}_i) + \sum_{j=1}^M g_j(\mathbf{Z}_j), \\ \text{s.t.} & \begin{cases} \mathbf{Z}_i = \sum_{j=1}^M \mathbf{G}_{j,i}(\mathbf{Y}_j), \\ \vdots, \\ \mathbf{Z}_M = \sum_{i=1}^N \mathbf{G}_{M,i}(\mathbf{Y}_i). \end{cases} \end{aligned} \quad (6)$$

where $\mathbf{G}_{j,i}$ ($i = 1, \dots, N, j = 1, \dots, M$) are linear operators. The preconditioned primal-dual splitting method (P-PDS) solves Prob. (6) by the following iterative procedures:

$$\begin{aligned} \tilde{\mathbf{Y}}_1 &\leftarrow \mathbf{Y}_1^{(t)} - \gamma_{1,1} \sum_{j=1}^M \mathbf{G}_{j,1}^*(\mathbf{Z}_j^{(t)}), \\ \mathbf{Y}_1^{(t+1)} &\leftarrow \text{prox}_{\gamma_{1,1} f_1}(\tilde{\mathbf{Y}}_1), \\ &\vdots \\ \tilde{\mathbf{Y}}_N &\leftarrow \mathbf{Y}_N^{(t)} - \gamma_{1,N} \sum_{j=1}^M \mathbf{G}_{j,N}^*(\mathbf{Z}_j^{(t)}), \\ \mathbf{Y}_N^{(t+1)} &\leftarrow \text{prox}_{\gamma_{1,N} f_N}(\tilde{\mathbf{Y}}_N), \\ \tilde{\mathbf{Z}}_1 &\leftarrow \mathbf{Z}_1^{(t)} + \gamma_{2,1} \sum_{i=1}^N \mathbf{G}_{1,i}(2\mathbf{Y}_i^{(t+1)} - \mathbf{Y}_i^{(t)}), \\ \mathbf{Z}_1^{(t+1)} &\leftarrow \text{prox}_{\gamma_{2,1} g_1^*}(\tilde{\mathbf{Z}}_1), \\ &\vdots \\ \tilde{\mathbf{Z}}_M &\leftarrow \mathbf{Z}_M^{(t)} + \gamma_{2,M} \sum_{i=1}^N \mathbf{G}_{M,i}(2\mathbf{Y}_i^{(t+1)} - \mathbf{Y}_i^{(t)}), \\ \mathbf{Z}_M^{(t+1)} &\leftarrow \text{prox}_{\gamma_{2,M} g_M^*}(\tilde{\mathbf{Z}}_M), \end{aligned} \quad (7)$$

where $\gamma_{1,i}$ ($i = 1, \dots, N$) and $\gamma_{2,j}$ ($j = 1, \dots, M$) are the stepsize parameters. The stepsize parameters can be determined automatically as follows [38], [39]:

$$\gamma_{1,i} = \frac{1}{\sum_{j=1}^M \|\mathbf{G}_{j,i}\|_{\text{op}}^2}, \quad \gamma_{2,j} = \frac{1}{N}, \quad (8)$$

where $\|\cdot\|_{\text{op}}$ is the operator norm defined by

$$\|\mathbf{G}\|_{\text{op}} := \sup_{\mathbf{X} \neq \mathbf{O}} \frac{\|\mathbf{G}(\mathbf{X})\|_F}{\|\mathbf{X}\|_F}. \quad (9)$$

Each step of the P-PDS algorithm consists only of the proximity operators and linear operators, leading to an efficient algorithm.

D. Regularizations for an HS image

This section introduces the regularizations for an HS image $\mathbf{H} \in \mathbb{R}^{l \times n_1 n_2}$. Let $\mathbf{D}_v : \mathbb{R}^{l \times n_1 n_2} \rightarrow \mathbb{R}^{l \times n_1 n_2}$, $\mathbf{D}_h : \mathbb{R}^{l \times n_1 n_2} \rightarrow \mathbb{R}^{l \times n_1 n_2}$, and $\mathbf{D}_b : \mathbb{R}^{l \times n_1 n_2} \rightarrow \mathbb{R}^{l \times n_1 n_2}$ be respectively vertical, horizontal, and spectral difference operators, which are given by

$$[\mathbf{D}_v(\mathbf{H})]_{i,j,k} := \begin{cases} [\mathbf{H}]_{i+1,j,k} - [\mathbf{H}]_{i,j,k} & \text{if } i < n_1, \\ 0 & \text{otherwise,} \end{cases} \quad (10)$$

$$[\mathbf{D}_h(\mathbf{H})]_{i,j,k} := \begin{cases} [\mathbf{H}]_{i,j+1,k} - [\mathbf{H}]_{i,j,k} & \text{if } j < n_2, \\ 0 & \text{otherwise,} \end{cases} \quad (11)$$

$$[\mathbf{D}_b(\mathbf{H})]_{i,j,k} := \begin{cases} [\mathbf{H}]_{i,j,k+1} - [\mathbf{H}]_{i,j,k} & \text{if } k < l, \\ 0 & \text{otherwise.} \end{cases} \quad (12)$$

Then, HTV [30], SSTV [33], and HSSTV [34] are as follows:

$$\text{HTV}(\mathbf{H}) := \|\mathbf{D}(\mathbf{H})\|_{1,2,c}, \quad (13)$$

$$\text{SSTV}(\mathbf{H}) := \|\mathbf{D}(\mathbf{D}_b(\mathbf{H}))\|_1, \quad (14)$$

$$\text{HSSTV}(\mathbf{H}) := \|\mathbf{A}_\omega(\mathbf{H})\|_1, \quad (15)$$

where \mathbf{D} is the spatial difference operator:

$$\mathbf{D}(\mathbf{H}) := \begin{bmatrix} \mathbf{D}_v(\mathbf{H}) \\ \mathbf{D}_h(\mathbf{H}) \end{bmatrix}, \quad (16)$$

and \mathbf{A}_ω is a combination of spatial and spatio-spectral difference operators with a balancing parameter $\omega \geq 0$:

$$\mathbf{A}_\omega(\mathbf{H}) := \begin{bmatrix} \mathbf{D}(\mathbf{D}_b(\mathbf{H})) \\ \omega \mathbf{D}(\mathbf{H}) \end{bmatrix}. \quad (17)$$

HTV captures spectral correlations by taking into account the sparsity of spatial differences grouped by the spectral direction. However, it does not directly evaluate for spectral differences, resulting in spatial oversmoothing. SSTV captures piecewise smoothness in the spectral direction by evaluating spatial differences through spectral differences (spatio-spectral difference). However, it does not sufficiently evaluate direct spatial piecewise smoothness, resulting in residual noise and artifacts. By evaluating both spatio-spectral and direct spatial differences, HSSTV can effectively remove noise and artifacts that would remain when evaluating spatio-spectral differences only. SSTV and HSSTV are more powerful regularizations than HTV because they evaluate both spatial and spectral directions.

III. RELATED WORKS

In this section, we review several existing unmixing methods that are closely related to our method. Let $\mathbf{A} \in \mathbb{R}^{l \times m}$, $\mathbf{X} \in \mathbb{R}^{m \times n}$, and $\mathbf{N} \in \mathbb{R}^{l \times n}$ be an endmember library, an abundance matrix, and Gaussian noise, respectively. Then, the observed HS image \mathbf{Y} is modeled according to LMM as follows:

$$\mathbf{Y} = \mathbf{A}\mathbf{X} + \mathbf{N}. \quad (18)$$

A. Collaborative Sparse Unmixing by Variable Splitting and Augmented Lagrangian (CLSUnSAL) [14]

CLSUnSAL estimates \mathbf{X} by solving the following optimization problem:

$$\min_{\mathbf{X} \in \mathbb{R}_+^{m \times n}} \frac{1}{2} \|\mathbf{Y} - \mathbf{A}\mathbf{X}\|_F^2 + \lambda \|\mathbf{X}\|_{1,2,r}. \quad (19)$$

Here, $\lambda > 0$ is a hyperparameter that balances each term. The first term serves as data fidelity. The second term is a regularization that evaluates the row sparsity of the abundance maps \mathbf{X} , called the joint-sparse regularization, which is based on the assumption that a mixel only contains a few endmembers compared with the large library.

B. Joint-Sparsity and Total Variation (JSTV) [15]

JSTV explicitly deals with the mixed noise of Gaussian noise \mathbf{N} and sparse noise \mathbf{S} , and then solves the following optimization problem:

$$\min_{\mathbf{X} \in \mathbb{R}_+^{m \times n}, \mathbf{S} \in \mathbb{R}^{l \times n}} \frac{1}{2} \|\mathbf{Y} - (\mathbf{A}\mathbf{X} + \mathbf{S})\|_F^2 + \lambda_1 \|\mathbf{X}\|_{1,2,r} + \lambda_2 \|\mathbf{D}(\mathbf{X})\|_1 + \lambda_3 \|\mathbf{S}\|_1 \quad (20)$$

Here, $\lambda_1 > 0$, $\lambda_2 > 0$, and $\lambda_3 > 0$ are hyperparameters that balance each term. The first term serves as data fidelity. The second and third terms are joint-sparse and piecewise-smooth regularizations for the abundance maps, respectively. The fourth term evaluates the sparsity of \mathbf{S} .

C. Row-Sparsity Spectral Unmixing via Total Variation (RSSUn-TV) [18]

RSSUn-TV solves the following optimization problem:

$$\min_{\mathbf{X} \in \mathbb{R}_+^{m \times n}} \frac{1}{2} \|\mathbf{Y} - \mathbf{A}\mathbf{X}\|_F^2 + \lambda_1 \|\mathbf{X}\|_{0,2,r} + \lambda_2 \|\mathbf{D}(\mathbf{X})\|_1 \quad (21)$$

where $\|\mathbf{X}\|_{0,2,r}$ counts the number of nonzero rows in matrix \mathbf{X} , i.e., $\|\mathbf{X}\|_{0,2,r} = \sum_i 1(\sqrt{\sum_j \mathbf{X}_{i,j}^2} > 0)$. Here, $\lambda_1 > 0$ and $\lambda_2 > 0$ are hyperparameters that balance each term. The first term serves as data fidelity. The second term evaluates the sparsity along the rows of the abundance maps. The third term evaluates the piecewise smoothness of \mathbf{X} . The $\ell_{0,2}$ -norm is difficult to optimize because of its nonconvexity.

D. Local-Global-Based Sparse Regression Unmixing Method (LGSU) [21]

LGSU captures the superpixel-wise sparsity and the global sparsity of abundance maps. First, LGSU separates HS images into a set of K homogeneous segments. Based on the segmentation, the unmixing problem is formulated as the following optimization problem:

$$\min_{\mathbf{X} \in \mathbb{R}_+^{m \times n}} \frac{1}{2} \|\mathbf{Y} - \mathbf{A}\mathbf{X}\|_F^2 + \lambda_1 \sum_{i=1}^K \mathcal{I}_i \|\mathbf{W}_1^{[i]} \odot \mathbf{X}^{[i]}\|_1 + \lambda_2 \|\mathbf{W}_2 \odot \mathbf{X}\|_1 \quad (22)$$

where $\lambda_1 > 0$ and $\lambda_2 > 0$ are hyperparameters that balance each term. The first term guarantees the data fidelity to \mathbf{Y} . The second and third terms promote the superpixel-wise sparsity and the global sparsity using the operators $\|\mathbf{W}_1^{[i]} \odot \cdot\|_1$ and $\|\mathbf{W}_2 \odot \cdot\|_1$ (\odot is element-wise multiplication), where $\mathbf{W}_1^{[i]}$ and \mathbf{W}_2 denote reweighting matrices controlling the row sparsity of $\mathbf{X}^{[i]}$ and \mathbf{X} , respectively. Here, \mathcal{I}_i is the homogeneity of the i th superpixel and $\mathbf{X}^{[i]}$ denotes the abundance of i th superpixel. For more detailed definitions and descriptions, see [21].

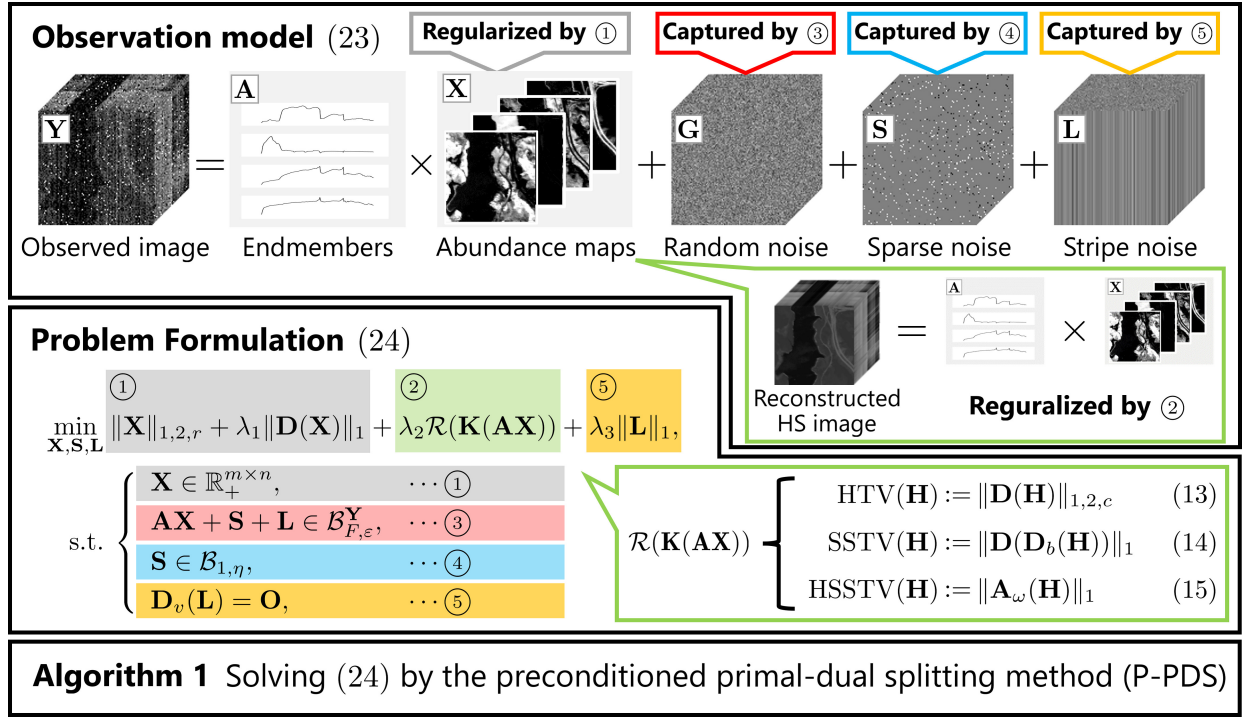


Fig. 2. Illustration of the proposed method, i.e., RCHU.

IV. PROPOSED METHOD

A general diagram of the proposed method, RCHU, is shown in Fig. 2. In the following, we first introduce an observation model with three types of noise. Based on the model, we then formulate the unmixing problem as a constrained convex optimization problem. Finally, we derive a P-PDS-based algorithm for efficiently solving the optimization problem.

A. Problem Formulation

Let \mathbf{N} , \mathbf{S} , and \mathbf{L} be Gaussian noise, sparse noise, and stripe noise, respectively. We consider the following observation model:

$$\mathbf{Y} = \mathbf{A}\mathbf{X} + \mathbf{N} + \mathbf{S} + \mathbf{L}. \quad (23)$$

Based on Eq. (23), we formulate the unmixing problem as the following constrained convex optimization problem:

$$\begin{aligned} \min_{\mathbf{X}, \mathbf{S}, \mathbf{L}} \quad & \|\mathbf{X}\|_{1,2,r} + \lambda_1 \|\mathbf{D}(\mathbf{X})\|_1 + \lambda_2 \mathcal{R}(\mathbf{K}(\mathbf{A}\mathbf{X})) + \lambda_3 \|\mathbf{L}\|_1, \\ \text{s.t.} \quad & \begin{cases} \mathbf{X} \in \mathbb{R}_+^{m \times n}, \\ \mathbf{A}\mathbf{X} + \mathbf{S} + \mathbf{L} \in \mathcal{B}_{F,\varepsilon}^{\mathbf{Y}}, \\ \mathbf{S} \in \mathcal{B}_{1,\eta}, \\ \mathbf{D}_v(\mathbf{L}) = \mathbf{O}, \end{cases} \end{aligned} \quad (24)$$

where $\lambda_1 > 0$, $\lambda_2 > 0$, and $\lambda_3 > 0$ are hyperparameters that balance each term. The first term is the joint-sparse regularization that evaluates the row sparsity of abundance maps \mathbf{X} . The second term promotes the piecewise smoothness of \mathbf{X} . The first constraint guarantees the non-negativity of \mathbf{X} .

The third term is the regularization of the reconstructed HS image. In this paper, we focus on three reconstructed-image

TABLE I
THE SPECIFIC FUNCTION \mathcal{R} AND LINEAR OPERATOR \mathbf{K} IN EACH
RECONSTRUCTED-IMAGE REGULARIZATION

Regularizations	\mathcal{R}	\mathbf{K}
HTV (Eq. (13))	$\ \cdot\ _{1,2,c}$	\mathbf{D}
SSTV (Eq. (14))	$\ \cdot\ _1$	$\mathbf{D} \circ \mathbf{D}_b$
HSSTV (Eq. (15))	$\ \cdot\ _1$	\mathbf{A}_ω

regularizations: HTV in (13), SSTV in (14), and HSSTV in (15). In each case, \mathcal{R} and \mathbf{K} are defined as shown in Tab. I. By further generalizing the third term, RCHU can incorporate other regularizations proposed, e.g., in [35], [36].

The second constraint serves as data fidelity to the observed HS image \mathbf{Y} with the Frobenius norm ball $\mathcal{B}_{F,\varepsilon}^{\mathbf{Y}}$ with the center \mathbf{Y} and radius ε , defined by

$$\mathcal{B}_{F,\varepsilon}^{\mathbf{Y}} := \{\mathbf{X} \mid \|\mathbf{Y} - \mathbf{X}\|_F \leq \varepsilon\}. \quad (25)$$

The third constraint evaluates the sparsity of \mathbf{S} with the ℓ_1 -norm ball $\mathcal{B}_{1,\eta}$ with center \mathbf{O} and radius η , defined by

$$\mathcal{B}_{1,\eta} := \{\mathbf{X} \mid \|\mathbf{X}\|_1 \leq \eta\}. \quad (26)$$

Using such constraints instead of data-fidelity and sparse terms make it easy to adjust hyperparameters since the parameter can be determined based only on noise intensity. Indeed, this kind of constrained formulation has played an important role in facilitating the parameter setup of signal recovery problems [41]–[45].

The third term controls the intensity of stripe noise \mathbf{L} and the fourth constraint captures the vertical flatness property by imposing zero to the vertical gradient of \mathbf{L} . The term and constraint effectively characterize stripe noise [29].

TABLE II
THE STEPSIZES $\gamma_1, \gamma_2, \gamma_3$, AND γ_4 FOR EACH RECONSTRUCTED-IMAGE REGULARIZATION

Regularizations	γ_1	γ_2	γ_3	γ_4
HTV (Eq. (13))	$\frac{1}{9+9\ \mathbf{A}\ _{\text{op}}^2}$	1	$\frac{1}{5}$	$\frac{1}{3}$
SSTV (Eq. (14))	$\frac{1}{9+17\ \mathbf{A}\ _{\text{op}}^2}$	1	$\frac{1}{5}$	$\frac{1}{3}$
HSSTV (Eq. (15))	$\frac{1}{9+(17+8\omega^2)\ \mathbf{A}\ _{\text{op}}^2}$	1	$\frac{1}{5}$	$\frac{1}{3}$

B. Optimization Algorithm

For solving Prob. (24) by an algorithm based on P-PDS, we need to transform Prob. (24) into Prob. (6). First, using the indicator function (see (1) for the definition), Prob. (24) are rewritten as follows:

$$\begin{aligned} \min_{\mathbf{X}, \mathbf{S}, \mathbf{L}} & \|\mathbf{X}\|_{1,2,r} + \lambda_1 \|\mathbf{D}(\mathbf{X})\|_1 + \lambda_2 \mathcal{R}(\mathbf{K} \circ \mathbf{A}(\mathbf{X})) + \lambda_3 \|\mathbf{L}\|_1 \\ & + \iota_{\mathbb{R}^{m \times n}}(\mathbf{X}) + \iota_{\mathcal{B}_{F,\varepsilon}^{\mathbf{Y}}}(\mathbf{A}\mathbf{X} + \mathbf{S} + \mathbf{L}) \\ & + \iota_{\mathcal{B}_{1,\eta}}(\mathbf{S}) + \iota_{\{\mathbf{O}\}}(\mathbf{D}_v(\mathbf{L})), \end{aligned} \quad (27)$$

where $\mathbf{K} \circ \mathbf{A}$ is the composite operator of \mathbf{K} and \mathbf{A} , i.e., $\mathbf{K} \circ \mathbf{A}(\mathbf{X}) = \mathbf{K}(\mathbf{A}\mathbf{X})$. Introducing auxiliary variables $\mathbf{Z}_1, \mathbf{Z}_2, \mathbf{Z}_3, \mathbf{Z}_4$, and \mathbf{Z}_5 , we can transform Prob. (27) into the following equivalent problem:

$$\begin{aligned} \min_{\substack{\mathbf{X}, \mathbf{S}, \mathbf{L}, \\ \mathbf{Z}_1, \dots, \mathbf{Z}_5}} & \iota_{\mathbb{R}^{m \times n}}(\mathbf{X}) + \iota_{\mathcal{B}_{1,\eta}}(\mathbf{S}) + \lambda_3 \|\mathbf{L}\|_1 + \|\mathbf{Z}_1\|_{1,2,r} \\ & + \lambda_1 \|\mathbf{Z}_2\|_1 + \lambda_2 \mathcal{R}(\mathbf{Z}_3) + \iota_{\mathcal{B}_{F,\varepsilon}^{\mathbf{Y}}}(\mathbf{Z}_4) + \iota_{\{\mathbf{O}\}}(\mathbf{Z}_5) \\ \text{s.t.} & \begin{cases} \mathbf{Z}_1 = \mathbf{X}, \\ \mathbf{Z}_2 = \mathbf{D}(\mathbf{X}), \\ \mathbf{Z}_3 = \mathbf{K} \circ \mathbf{A}(\mathbf{X}), \\ \mathbf{Z}_4 = \mathbf{A}\mathbf{X} + \mathbf{S} + \mathbf{L}, \\ \mathbf{Z}_5 = \mathbf{D}_v(\mathbf{L}). \end{cases} \end{aligned} \quad (28)$$

Finally, by defining $f_1(\mathbf{X}) = \iota_{\mathbb{R}^{m \times n}}(\mathbf{X})$, $f_2(\mathbf{S}) = \iota_{\mathcal{B}_{1,\eta}}(\mathbf{S})$, $f_3(\mathbf{L}) = \lambda_3 \|\mathbf{L}\|_1$, $g_1(\mathbf{Z}_1) = \|\mathbf{Z}_1\|_{1,2,r}$, $g_2(\mathbf{Z}_2) = \lambda_1 \|\mathbf{Z}_2\|_1$, $g_3(\mathbf{Z}_3) = \lambda_2 \mathcal{R}(\mathbf{Z}_3)$, $g_4(\mathbf{Z}_4) = \iota_{\mathcal{B}_{F,\varepsilon}^{\mathbf{Y}}}(\mathbf{Z}_4)$, and $g_5(\mathbf{Z}_5) = \iota_{\{\mathbf{O}\}}(\mathbf{Z}_5)$, Prob. (6) is reduced to Prob. (28), i.e., Prob. (24).

The algorithm for solving Prob. (24) is summarized in Algorithm 1. \mathbf{K} in steps 2 and 12, and \mathcal{R} in step 13 depend on what regularization is adopted, as shown in Tab. I. The proximity operators are calculated as follows:

$$[\text{prox}_{\gamma \iota_{\mathbb{R}^{m \times n}}}(\mathbf{X})]_{i,j} = \max(0, \mathbf{X}_{i,j}), \quad (29)$$

$$[\text{prox}_{\gamma \|\cdot\|_1}(\mathbf{X})]_{i,j} = \text{sign}(\mathbf{X}_{i,j}) \max(|\mathbf{X}_{i,j}| - \gamma, 0), \quad (30)$$

$$[\text{prox}_{\gamma \|\cdot\|_{1,2,r}}(\mathbf{X})]_{i,j} = \max(1 - \frac{\gamma}{\sqrt{\sum_j \mathbf{X}_{i,j}^2}}, 0) \mathbf{X}_{i,j}, \quad (31)$$

$$[\text{prox}_{\gamma \|\cdot\|_{1,2,c}}(\mathbf{X})]_{i,j} = \max(1 - \frac{\gamma}{\sqrt{\sum_i \mathbf{X}_{i,j}^2}}, 0) \mathbf{X}_{i,j}, \quad (32)$$

$$\text{prox}_{\gamma \iota_{\mathcal{B}_{F,\varepsilon}^{\mathbf{Y}}}}(\mathbf{X}) = \begin{cases} \mathbf{X}, & \text{if } \mathbf{X} \in \mathcal{B}_{F,\varepsilon}^{\mathbf{Y}}, \\ \mathbf{Y} + \frac{\varepsilon(\mathbf{X}-\mathbf{Y})}{\|\mathbf{X}-\mathbf{Y}\|_F}, & \text{otherwise,} \end{cases} \quad (33)$$

$$\text{prox}_{\gamma \iota_{\{\mathbf{O}\}}}(\mathbf{X}) = \mathbf{O}. \quad (34)$$

Algorithm 1 A P-PDS-based algorithm for solving Prob. (24)

Input: \mathbf{Y} , λ_1 , λ_2 , λ_3 , ε , and α

Output: $\mathbf{X}^{(t)}$, $\mathbf{S}^{(t)}$, $\mathbf{L}^{(t)}$

```

1: Initialize  $\mathbf{A}^{(0)}$ ,  $\mathbf{Z}_1$ ,  $\mathbf{Z}_2$ ,  $\mathbf{Z}_3$ ,  $\mathbf{Z}_4$ , and  $\mathbf{Z}_5$ ;
2: Set  $\gamma_1, \gamma_2, \gamma_3$ , and  $\gamma_4$  as in Tab. II;
3: while until a stopping criterion is satisfied do
4:    $\tilde{\mathbf{X}} \leftarrow \mathbf{Z}_1^{(t)} + \mathbf{D}^*(\mathbf{Z}_2^{(t)}) + \mathbf{A}^*(\mathbf{K}^*(\mathbf{Z}_3^{(t)})) + \mathbf{A}^*\mathbf{Z}_4^{(t)}$ ;
5:    $\tilde{\mathbf{X}} \leftarrow \mathbf{X}^{(t)} - \gamma_1 \tilde{\mathbf{X}}$ ;
6:    $\mathbf{X}^{(t+1)} \leftarrow \text{prox}_{\gamma_1 \iota_{\mathbb{R}^{m \times n}}}(\tilde{\mathbf{X}})$  by (29);
7:    $\tilde{\mathbf{S}} \leftarrow \mathbf{S}^{(t)} - \gamma_2 \mathbf{Z}_4^{(t)}$ ;
8:    $\mathbf{S}^{(t+1)} \leftarrow \text{prox}_{\gamma_2 \iota_{\mathcal{B}_{1,\eta}}}(\tilde{\mathbf{S}})$ ;
9:    $\tilde{\mathbf{L}} \leftarrow \mathbf{L}^{(t)} - \gamma_3(\mathbf{Z}_4^{(t)} + \mathbf{D}_v^*(\mathbf{Z}_5^{(t)}))$ ;
10:   $\mathbf{L}^{(t+1)} \leftarrow \text{prox}_{\gamma_3 \lambda_3 \|\cdot\|_1}(\tilde{\mathbf{L}})$  by (30);
11:   $\tilde{\mathbf{Z}}_1 \leftarrow \mathbf{Z}_1^{(t)} + \gamma_4(2\mathbf{X}^{(t+1)} - \mathbf{X}^{(t)})$ ;
12:   $\mathbf{Z}_1^{(t+1)} \leftarrow \mathbf{Z}_1^{(t)} - \gamma_4 \text{prox}_{\frac{1}{\gamma_4} \|\cdot\|_{1,2,r}}(\frac{\tilde{\mathbf{Z}}_1}{\gamma_4})$  by (31);
13:   $\tilde{\mathbf{Z}}_2 \leftarrow \mathbf{Z}_2^{(t)} + \gamma_4 \mathbf{D}(2\mathbf{X}^{(t+1)} - \mathbf{X}^{(t)})$ ;
14:   $\mathbf{Z}_2^{(t+1)} \leftarrow \mathbf{Z}_2^{(t)} - \gamma_4 \text{prox}_{\frac{\lambda_1}{\gamma_4} \|\cdot\|_1}(\frac{\tilde{\mathbf{Z}}_2}{\gamma_4})$  by (30);
15:   $\tilde{\mathbf{Z}}_3 \leftarrow \mathbf{Z}_3^{(t)} + \gamma_4 \mathbf{K}(\mathbf{A}(2\mathbf{X}^{(t+1)} - \mathbf{X}^{(t)}))$ ;
16:   $\mathbf{Z}_3^{(t+1)} \leftarrow \mathbf{Z}_3^{(t)} - \gamma_4 \text{prox}_{\frac{\lambda_2}{\gamma_4} \mathcal{R}}(\frac{\tilde{\mathbf{Z}}_3}{\gamma_4})$  by (30) or (32);
17:   $\tilde{\mathbf{Z}}_4' \leftarrow 2(\mathbf{A}\mathbf{X}^{(t+1)} + \mathbf{S}^{(t+1)} + \mathbf{L}^{(t+1)})$ ;
18:   $\tilde{\mathbf{Z}}_4 \leftarrow \mathbf{A}\mathbf{X}^{(t)} + \mathbf{S}^{(t)} + \mathbf{L}^{(t)}$ ;
19:   $\tilde{\mathbf{Z}}_4 \leftarrow \mathbf{Z}_4^{(t)} + \gamma_4(\tilde{\mathbf{Z}}_4' - \tilde{\mathbf{Z}}_4)$ ;
20:   $\mathbf{Z}_4^{(t+1)} \leftarrow \mathbf{Z}_4^{(t)} - \gamma_4 \text{prox}_{\frac{1}{\gamma_4} \iota_{\mathcal{B}_{F,\varepsilon}^{\mathbf{Y}}}}(\frac{\tilde{\mathbf{Z}}_4}{\gamma_4})$  by (33);
21:   $\tilde{\mathbf{Z}}_5 \leftarrow \mathbf{Z}_5^{(t)} + \gamma_4 \mathbf{D}_v(2\mathbf{L}^{(t+1)} - \mathbf{L}^{(t)})$ ;
22:   $\mathbf{Z}_5^{(t+1)} \leftarrow \mathbf{Z}_5^{(t)} - \gamma_4 \text{prox}_{\frac{1}{\gamma_4} \iota_{\{\mathbf{O}\}}}}(\frac{\tilde{\mathbf{Z}}_5}{\gamma_4})$  by (34);
23:   $t \leftarrow t + 1$ ;
24: end while

```

The proximity operator of $\iota_{\gamma \mathcal{B}_{1,\eta}}(\mathbf{X})$ can be efficiently computed by the ℓ_1 -ball projection algorithm [46]. The step-sizes are determined based on the automatic adjustment method [38], [39] as shown in Tab. II.

V. EXPERIMENTS

We demonstrate the effectiveness of the proposed non-blind unmixing method, i.e., RCHU through comprehensive experiments using two synthetic and one real HS images. Specifically, these experiments aim to validate that

- RCHU achieves good unmixing performance due to reconstructed-image regularizations,
- RCHU is robust to mixed noise, including stripe noise.

As described in the introduction, existing unmixing methods are classified into blind and non-blind, depending on whether the endmember library is given or not. Due to the different assumptions and the fact that blind unmixing methods require a non-blind unmixing step to obtain an initial estimate, it is difficult to fairly compare non-blind unmixing methods with blind ones. Therefore, we compare RCHU with four state-of-the-art non-blind unmixing methods: CLSUnSAL [14], JSTV [15], RSSUn-TV [18], and LGSU [21]. Tab. III shows the types of noise taken into account by these methods.

TABLE III
NOISE TAKEN INTO ACCOUNT BY EACH METHOD

Methods	Gaussian noise	Sparse noise	Stripe noise
CLSunSAL [14]	✓	-	-
JSTV [15]	✓	✓	-
RSSUn-TV [18]	✓	-	-
LGSU [21]	✓	-	-
RCHU (Ours)	✓	✓	✓

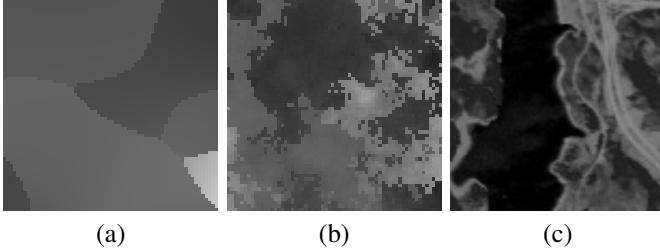


Fig. 3. Original HS images. (a): A synthetic image generated using a Legendre method. (b): A synthetic image generated using a spherical Gaussian method. (c): A real image (*Jasper Ridge*).

A. Data Description

1) *Synthetic HS Image 1*: We generated the first synthetic HS image with the size of $64 \times 64 \times 224$ using the HYperspectral Data Retrieval and Analysis (HYDRA) toolbox¹, which is developed by the Computational Intelligence group at the University of the Basque Country. The library of 10 endmembers and 224 bands was used for unmixing. We generated the four original abundance maps with the spatial size of 64×64 using the Legendre method. Fig. 3 (a) shows one band of the generated image.

2) *Synthetic HS Image 2*: We also generated the second synthetic HS image with size of $64 \times 64 \times 224$ using the HYDRA toolbox. The library of 10 endmembers and 224 bands was used for unmixing. We generated the four original abundance maps with the spatial size of 64×64 using the spherical Gaussian method. Fig. 3 (b) shows one band of the generated image.

3) *Real Image (Jasper Ridge)*: Real data experiments were conducted with the *Jasper Ridge* image (see Fig. 3 (c)), which is captured using an AVIRIS sensor in a rural area in California, USA. The spatial size of the original data is 512×614 pixels, and each pixel holds spectral information in 224 bands ranging from 380 nm to 2500 nm. After removing several noisy bands and cropping the image, we obtained the image with 100×100 pixels and 198 bands. *Jasper Ridge* contains four major endmembers²: "road," "soil," "water," and "tree" [47]. Adding the six endmembers, we used a total of 10 endmembers for the experiments.

B. Experimental Setup

HS images are often degraded by a mixture of various types of noise in real-noise scenarios. Thus, we consider the

following six combinations of Gaussian noise with different standard deviations σ , salt-and-pepper noise with different rate p_S , and stripe noise in both synthetic and real data experiments.

- Case 1: The observed HS image is contaminated by white Gaussian noise with the standard deviation $\sigma = 0.05$.
- Case 2: The observed HS image is contaminated by white Gaussian noise with the standard deviation $\sigma = 0.1$.
- Case 3: The observed HS image is contaminated by white Gaussian noise with the standard deviation $\sigma = 0.05$ and salt-and-pepper noise with the rate $p_S = 0.05$.
- Case 4: The observed HS image is contaminated by white Gaussian noise with the standard deviation $\sigma = 0.05$ and salt-and-pepper noise with the rate $p_S = 0.1$.
- Case 5: The observed HS image is contaminated by white Gaussian noise with the standard deviation $\sigma = 0.05$ and salt-and-pepper noise with the rate $p_S = 0.05$. In addition, the observed HS image is corrupted by vertical stripe noise whose intensity is random in the range $[-0.3, 0.3]$.
- Case 6: The observed HS image is contaminated by white Gaussian noise with the standard deviation $\sigma = 0.1$ and salt-and-pepper noise with the rate $p_S = 0.05$. In addition, the observed HS image is corrupted by vertical stripe noise whose intensity is random in the range $[-0.3, 0.3]$.

As the parameters of existing methods, we used the values recommended in each reference. The parameters of RCHU were set as $\lambda_1 = 2, \lambda_2 = 2$, and $\lambda_3 = 1$, which are adjusted to achieve the best performance. As the parameter of HSSTV, we adopted $\omega = 0.05$, which is recommended in [34]. The parameter η and ε were set as $\eta = 0.45p_S n l$ and $\varepsilon = 0.95\sigma\sqrt{(1-p_S)n l}$. The maximum iteration and the stopping criterion were set to 100,000 and $\frac{\|\mathbf{X}^{(t+1)} - \mathbf{X}^{(t)}\|_F}{\|\mathbf{X}^{(t+1)}\|_F} \leq 10^{-5}$, respectively.

For the quantitative evaluation of abundance maps, we used the signal reconstruction error (SRE):

$$\text{SRE[dB]} = 10 \log_{10} \left(\frac{\|\mathbf{X}\|_F^2}{\|\mathbf{X} - \hat{\mathbf{X}}\|_F^2} \right), \quad (35)$$

the root-mean-square error (RMSE):

$$\text{RMSE} = \sqrt{\frac{1}{mn} \|\mathbf{X} - \hat{\mathbf{X}}\|_F^2}, \quad (36)$$

and probability of success (Ps):

$$\text{Ps} = P \left(\frac{(\mathbf{X}_{i,j} - \hat{\mathbf{X}}_{i,j})^2}{(\mathbf{X}_{i,j})^2} \leq \text{threshold} \right), \quad (37)$$

where \mathbf{X} and $\hat{\mathbf{X}}$ denote the true and estimated abundance maps, respectively. SRE and RMSE evaluate the difference between the true and estimated abundance maps, with larger SRE or smaller RMSE indicating better-estimated performance. Ps is the probability that the relative error is less than a certain threshold. In this case, the threshold was set at 0.316, which is 5 dB.

¹https://www.ehu.es/ccwintco/index.php?title=Hyperspectral_Imagery_Synthesis_tools_for_MATLAB, accessed on Feb. 5, 2023

²True abundance maps are available from <http://lesun.weebly.com/hyperspectral-data-set.html>

TABLE IV
THE SRE, RMSE, Ps, MPSNR, AND MSSIM RESULTS IN THE EXPERIMENTS WITH THE SYNTHETIC HS IMAGE 1.

Noise	Evaluation Target	Measures	Methods						
			CLSunSAL [14]	JSTV [15]	RSSUn-TV [18]	LGSU [21]	RCHU (HTV)	RCHU (SSTV)	RCHU (HSSTV)
Case 1	Abundance	SRE	16.50	12.95	11.39	16.59	27.22	27.02	26.99
		RMSE	0.0590	0.0840	0.0992	0.0608	0.0173	<u>0.0177</u>	<u>0.0177</u>
		Ps	0.68	0.56	0.53	0.64	0.92	0.92	0.92
	Reconstructed HS image	MPSNR	41.26	39.94	39.70	41.19	<u>46.09</u>	44.49	46.26
Case 2	Abundance	MSSIM	0.9771	0.9706	0.9693	0.9754	0.9936	0.9906	<u>0.9940</u>
		SRE	12.81	7.83	7.13	12.73	<u>21.85</u>	21.84	22.12
		RMSE	0.0889	0.1424	0.1530	0.0923	<u>0.0318</u>	<u>0.0318</u>	0.0308
		Ps	0.55	0.41	0.40	0.52	<u>0.80</u>	<u>0.80</u>	0.81
Case 3	Abundance	MPSNR	36.13	34.51	34.42	35.39	<u>38.86</u>	37.91	39.19
		MSSIM	0.9322	0.9114	0.9101	0.9213	<u>0.9660</u>	0.9585	0.9692
		SRE	9.20	10.87	3.47	7.18	<u>25.76</u>	25.61	25.81
		RMSE	0.1275	0.1045	0.2088	0.1614	<u>0.0205</u>	0.0208	0.0203
Case 4	Abundance	Ps	0.46	0.51	0.29	0.39	0.89	0.89	0.90
		MPSNR	30.73	38.20	28.88	29.28	<u>43.69</u>	42.38	43.97
		MSSIM	0.8505	0.9573	0.8003	0.8115	<u>0.9884</u>	0.9844	0.9894
	Reconstructed HS image	SRE	11.42	11.97	5.72	10.72	26.40	26.04	<u>26.07</u>
Case 5	Abundance	RMSE	0.1018	0.0931	0.1720	0.1138	0.0190	0.0197	<u>0.0196</u>
		Ps	0.53	0.53	0.36	0.49	0.91	<u>0.90</u>	0.91
		MPSNR	33.82	39.02	31.94	32.73	<u>45.43</u>	43.64	45.58
	Reconstructed HS image	MSSIM	0.9026	0.9641	0.8688	0.8821	0.9926	0.9885	0.9930
Case 6	Abundance	SRE	10.68	7.86	4.85	9.61	<u>23.85</u>	23.71	24.00
		RMSE	0.1096	0.1418	0.1860	0.1264	<u>0.0252</u>	0.0255	0.0247
		Ps	0.50	0.43	0.34	0.46	<u>0.82</u>	<u>0.82</u>	0.84
	Reconstructed HS image	MPSNR	32.93	35.52	31.16	31.81	<u>41.33</u>	40.13	41.76
Case 7	Abundance	MSSIM	0.8908	0.9338	0.8534	0.8649	<u>0.9850</u>	0.9792	0.9870
		SRE	9.79	5.83	4.16	8.10	20.13	<u>19.72</u>	19.63
		RMSE	0.1209	0.1720	0.1981	0.1471	0.0377	<u>0.0393</u>	0.0396
		Ps	0.47	0.36	0.31	0.42	<u>0.79</u>	0.80	<u>0.82</u>
Case 8	Reconstructed HS image	MPSNR	31.85	32.35	30.13	30.62	<u>38.85</u>	36.95	39.44
		MSSIM	0.8615	0.8702	0.8191	0.8294	<u>0.9702</u>	0.9527	0.9753

For the quantitative evaluation of the reconstructed HS images, we used the mean peak signal-to-noise ratio overall bands (MPSNR):

$$\text{MPSNR}[\text{dB}] = \frac{1}{l} \sum_{i=1}^l 10 \log_{10} \left(\frac{n}{\|\mathbf{H}_{i,j} - \hat{\mathbf{H}}_{i,j}\|_F^2} \right), \quad (38)$$

where \mathbf{H} and $\hat{\mathbf{H}}$ are the ground-truth and reconstructed HS images, respectively. In addition, we adopted the mean structural similarity overall bands (MSSIM) [48]:

$$\text{MSSIM} = \frac{1}{l} \sum_{i=1}^l \text{SSIM}(\mathbf{H}_i, \hat{\mathbf{H}}_i), \quad (39)$$

where \mathbf{H}_i and $\hat{\mathbf{H}}_i$ are the i th bands of \mathbf{H} and $\hat{\mathbf{H}}$, respectively. Higher MPSNR and MSSIM values indicate better reconstruction results.

C. Experimental Results With Synthetic HS Images

Tables IV and V show the SRE, RMSE, Ps, MPSNR, and MSSIM results with the synthetic HS images generated using the Legendre method and spherical Gaussian methods,

respectively. The best and second-best results are highlighted in bold and underlined, respectively. JSTV and RSSUn-TV are worse in all cases. CLSunSAL was best in SRE and RMSE for Case 1 of the synthetic image, but degraded its performance as σ increased (see Case 2 of the synthetic image). In other cases, LGSU degraded its performance. In contrast, RCHU yielded the best SRE, RMSE, Ps, MPSNR, and MSSIM values for the cases where the HS image is contaminated with noise that can be handled by the existing methods (Cases 1 and 2 for CLSunSAL, RSSUn-TV, and LGSU, and Cases 1, 2, 3, and 4 for JSTV), except for Case 1 of the synthetic HS image. This indicates that the reconstructed-image regularizations can improve the unmixing performance. In addition, RCHU achieved the best performance for the other cases (Cases 5, 6). This is due to the fact that RCHU can handle all three types of noise. When comparing the reconstructed-image regularizations, SSTV and HSSTV performed better.

Figures 4 and 5 show the estimated abundance maps for the synthetic HS image 1 in Case 2 and Case 4, respectively. Figure 6 depicts the estimated abundance maps for the synthetic HS image 2 in Case 5. In Case 5, All abundance maps of CLSunSAL, JSTV, RSSUn-TV, and LGSU include residual

TABLE V
THE SRE, RMSE, Ps, MPSNR, AND MSSIM RESULTS IN THE EXPERIMENTS WITH THE SYNTHETIC HS IMAGE 2.

Noise	Evaluation Target	Measures	Methods						
			CLSUnSAL [14]	JSTV [15]	RSSUn-TV [18]	LGSU [21]	RCHU (HTV)	RCHU (SSTV)	RCHU (HSSTV)
Case 1	Abundance	SRE	10.57	9.39	8.70	6.50	9.95	9.98	9.96
		RMSE	0.1081	0.1239	0.1342	0.1694	0.1162	<u>0.1158</u>	0.1160
		Ps	0.60	0.52	0.49	0.54	0.78	0.79	0.79
	Reconstructed HS image	MPSNR	40.41	39.58	39.38	40.45	<u>42.12</u>	41.69	42.16
Case 2	Abundance	MSSIM	0.9870	0.9841	0.9833	0.9875	0.9926	0.9912	<u>0.9925</u>
		SRE	7.97	6.00	5.64	5.74	8.39	8.45	8.48
		RMSE	0.1459	0.1829	0.1907	0.1837	0.1390	<u>0.1381</u>	0.1376
		Ps	0.49	0.39	0.38	0.45	0.61	<u>0.62</u>	0.63
Case 3	Abundance	MPSNR	35.10	34.10	34.01	34.88	<u>36.25</u>	36.01	36.51
		MSSIM	0.9593	0.9485	0.9477	0.9562	<u>0.9715</u>	0.9693	0.9732
		SRE	6.22	8.43	3.02	3.73	9.70	9.77	<u>9.76</u>
		RMSE	0.1785	0.1384	0.2579	0.2465	0.1195	0.1186	<u>0.1187</u>
Case 4	Abundance	Ps	0.43	0.48	0.29	0.36	0.77	0.78	0.78
		MPSNR	29.97	37.94	28.63	28.98	<u>40.63</u>	40.20	40.75
		MSSIM	0.9093	0.9773	0.8775	0.8876	<u>0.9898</u>	0.9880	0.9899
	Reconstructed HS image	SRE	7.19	8.67	4.27	5.11	<u>9.73</u>	9.74	9.72
Case 5	Abundance	RMSE	0.1596	0.1346	0.2233	0.1986	<u>0.1192</u>	0.1190	<u>0.1192</u>
		Ps	0.47	0.50	0.34	0.42	0.78	0.79	<u>0.78</u>
		MPSNR	32.88	38.63	31.60	32.24	<u>41.30</u>	40.89	41.40
	Reconstructed HS image	MSSIM	0.9423	0.9806	0.9235	0.9331	0.9914	0.9898	0.9914
Case 6	Abundance	SRE	6.84	6.36	4.01	4.77	<u>9.00</u>	9.02	8.99
		RMSE	0.1661	0.1756	0.2301	0.2108	<u>0.1295</u>	0.1293	0.1297
		Ps	0.45	0.41	0.32	0.40	<u>0.74</u>	0.75	<u>0.74</u>
	Reconstructed HS image	MPSNR	32.34	35.46	31.00	31.55	<u>39.10</u>	38.40	39.32
Case 7	Abundance	MSSIM	0.9368	0.9640	0.9150	0.9242	<u>0.9880</u>	0.9850	0.9885
		SRE	6.46	4.62	3.37	4.16	<u>7.94</u>	7.97	7.92
		RMSE	0.1736	0.2146	0.2477	0.2298	<u>0.1464</u>	0.1459	0.1468
		Ps	0.43	0.34	0.30	0.37	<u>0.68</u>	0.69	<u>0.68</u>
Case 8	Reconstructed HS image	MPSNR	31.18	32.12	29.95	30.38	<u>35.97</u>	35.09	36.11
		MSSIM	0.9175	0.9246	0.8926	0.9012	<u>0.9735</u>	0.9641	0.9737

noise in Cases 2, 4, and 5 (see Figs. 4, 5, and 6 (b), (c), (d), and (e)). In particular, they do not take stripe noise into account, producing abundance maps greatly affected by stripe noise (see Fig. 6 (b), (c), (d), and (e)). In contrast, RCHU exactly estimated abundance maps regardless of what type of noise contaminates HS images (see Figs. 4, 5, and 6 (f), (g), and (h)).

Figures 7 and 8 display the reconstructed HS images of the synthetic image 1 in Case 2 and Case 4, respectively. Figure 9 depicts the reconstructed HS images of the synthetic image 2 in Case 5. CLSUnSAL, JSTV, RSSUn-TV, and LGSU resulted in Gaussian noise remaining in the reconstructed HS images in Case 2 (see Fig. 7 (c), (d), (e), and (f)). Moreover, in the reconstructed HS images of CLSUnSAL, JSTV, RSSUn-TV, and LGSU (see Fig. 9 (c), (d), (e), and (f)), we can see that residual stripe noise remains. On the other hand, RCHU produced clean reconstructed HS images due to the reconstructed-image regularizations.

D. Experiments With A Real HS Image

Table VI shows the SRE, RMSE, Ps, MPSNR, and MSSIM results for the real HS image cases. The best and second-best

results are highlighted in bold and underlined, respectively. CLSUnSAL, JSTV, and RSSUn-TV performed worse in all cases. LGSU was the best for SRE, RMSE, and Ps in Cases 1 and 2 of the real data experiments. The reason for this is that LGSU accurately calculates the homogeneities of *Jasper Ridge* and the local sparsity promoted by the homogeneities significantly enhances the unmixing performance in these cases. In other cases, LGSU degraded the performance because it is not robust to sparse and stripe noise. In contrast, RCHU achieved the best SRE, RMSE, Ps, MPSNR, and MSSIM performances for the cases where the HS image is contaminated by noise that can be handled by the existing methods (Cases 1 and 2 for CLSUnSAL, RSSUn-TV, and LGSU, and Cases 1, 2, 3, and 4 for JSTV), except for Case 1, 2. In addition, RCHU can handle all three types of noise, resulting in the best performance for the other cases (Cases 5, 6). When comparing reconstructed-image regularizations, HTV performed better. We speculate that this is because SSTV and HSSTV are effective for HS images that strictly follow the LMM (e.g., synthetic data), but are too strong for the real HS image.

Figures 10 and 11 depict the estimated abundance maps for the real image in Case 2 and Case 5, respectively. As shown

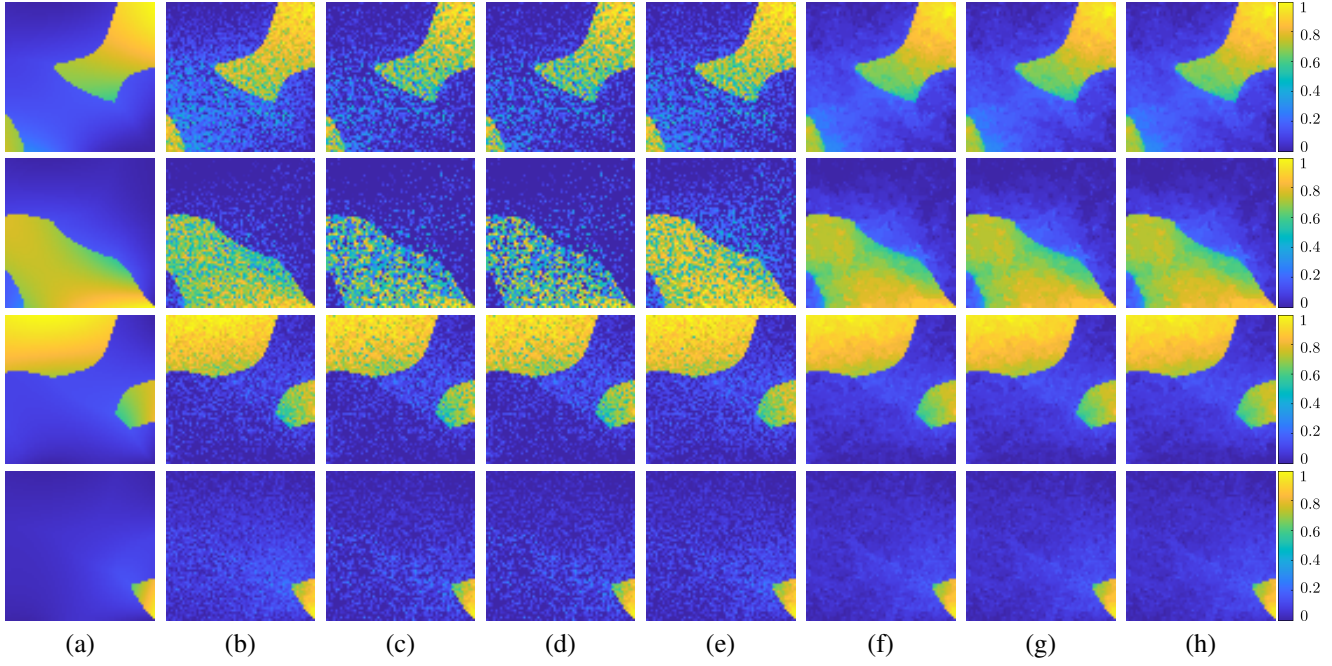


Fig. 4. Unmixing results of abundance maps for the synthetic data in Case 2. (a): Original abundance maps. (b): CLSUnSAL [14]. (c): JSTV [15]. (d): RSSUn-TV [18]. (e): LGSU [21]. (f): **RCHU (HTV)**. (g): **RCHU (SSTV)**. (h): **RCHU (HSSTV)**.

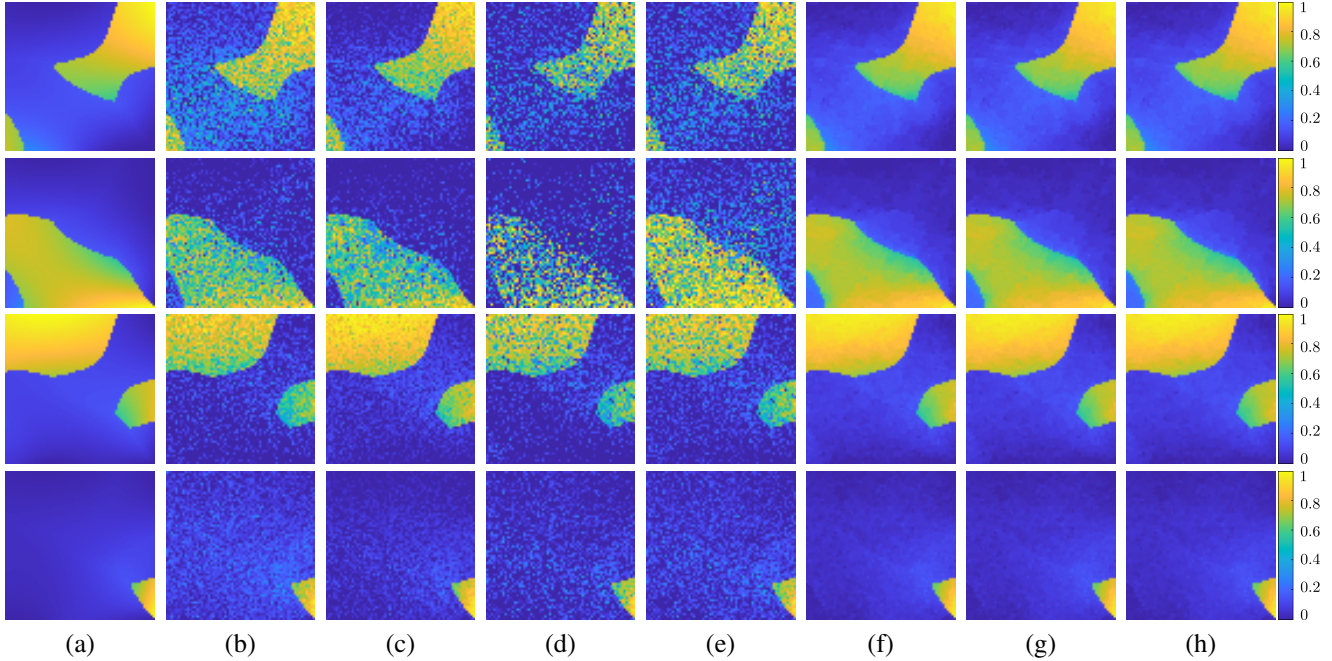


Fig. 5. Unmixing results of abundance maps for the synthetic data in Case 4. (a): Original abundance maps. (b): CLSUnSAL [14]. (c): JSTV [15]. (d): RSSUn-TV [18]. (e): LGSU [21]. (f): **RCHU (HTV)**. (g): **RCHU (SSTV)**. (h): **RCHU (HSSTV)**.

in Fig. 10 (b), (c), (d), and (e), if HS images are contaminated by Gaussian noise with large sigma, all existing methods degraded their performance. Although LGSU achieved the best SRE, RMSE, and Ps in Case 2 of the real data experiments, it yielded abundance maps with residual noise (see Fig. 10 (e)). In Case 5, the abundance maps estimated by CLSUnSAL, JSTV, RSSUn-TV, and LGSU include residual noise, especially stripe noise (see Fig. 11, (b), (c), (d), and (e)). This indicates that they do not handle the stripe noise. In contrast,

RCHU exactly estimated the abundance maps even under the conditions assumed by the existing methods, e.g. when the observed HS images are only contaminated by Gaussian noise (see Fig. 10). Furthermore, RCHU estimated the abundance maps by removing not only Gaussian and sparse noise but also stripe noise cleanly.

Figures 12 and 13 show the reconstructed HS images of *Jasper Ridge* in Case 2 and Case 5, respectively. CLSUnSAL, JSTV, RSSUn-TV, and LGSU resulted in noise remaining in

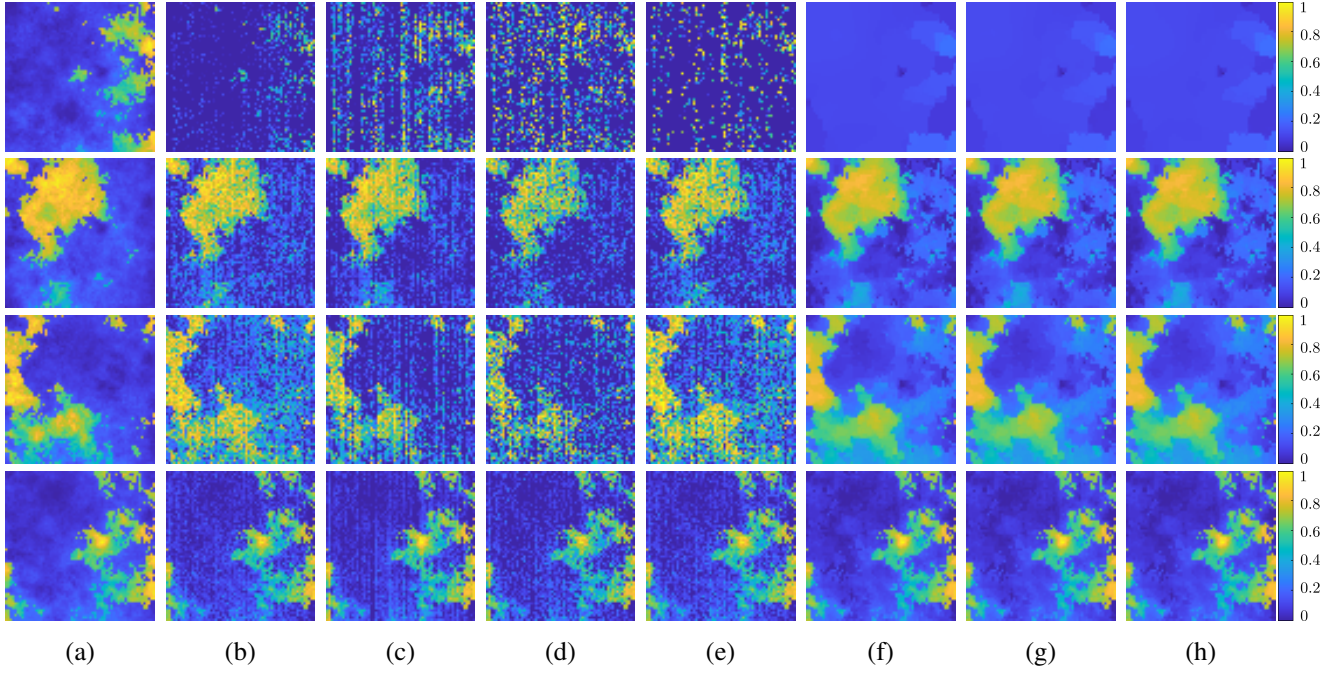


Fig. 6. Unmixing results of abundance maps for the synthetic data in Case 5. (a): Original abundance maps. (b): CLSUnSAL [14]. (c): JSTV [15]. (d): RSSUn-TV [18]. (e): LGSU [21]. (f): **RCHU (HTV)**. (g): **RCHU (SSTV)**. (h): **RCHU (HSSTV)**.

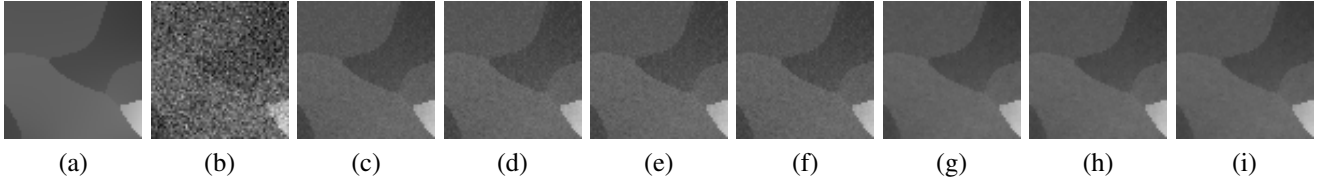


Fig. 7. Reconstructed HS image results for the synthetic data in Case 2. (a): Original HS image. (b): Noisy image. (c): CLSUnSAL [14]. (d): JSTV [15]. (e): RSSUn-TV [18]. (f): LGSU [21]. (g): **RCHU (HTV)**. (h): **RCHU (SSTV)**. (i): **RCHU (HSSTV)**.

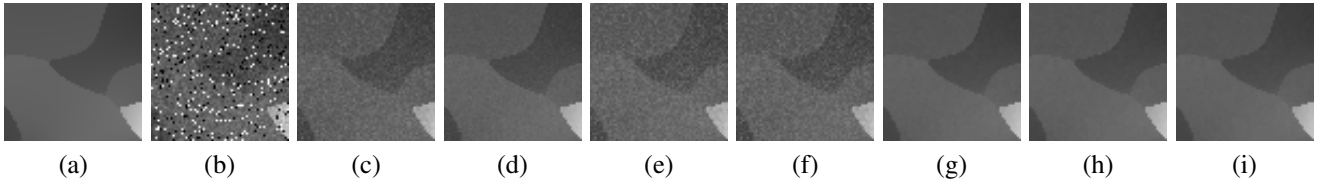


Fig. 8. Reconstructed HS image results for the synthetic data in Case 4. (a): Original HS image. (b): Noisy image. (c): CLSUnSAL [14]. (d): JSTV [15]. (e): RSSUn-TV [18]. (f): LGSU [21]. (g): **RCHU (HTV)**. (h): **RCHU (SSTV)**. (i): **RCHU (HSSTV)**.

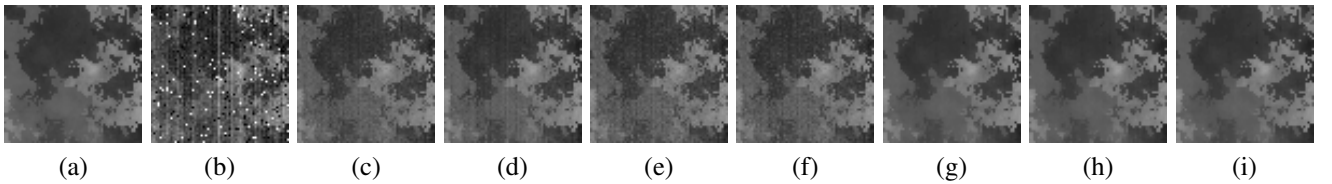


Fig. 9. Reconstructed HS image results for the synthetic data in Case 5. (a): Original HS image. (b): Noisy image. (c): CLSUnSAL [14]. (d): JSTV [15]. (e): RSSUn-TV [18]. (f): LGSU [21]. (g): **RCHU (HTV)**. (h): **RCHU (SSTV)**. (i): **RCHU (HSSTV)**.

the reconstructed HS images (see Figs. 12 and 13 (c), (d), (e), and (f)). In particular, they cannot handle stripe noise, and thus did not completely remove it in Case 5 (see Fig. 13 (c), (d), (e), and (f)). On the other hand, RCHU reconstructed the HS image cleanly (see Figs. 12 and 13 (g), (h), and (i)). This verifies the effectiveness of the reconstructed-image regularization.

E. Summary

We summarize the experimental discussion as follows .

- From the results of experiments in Case 1, Case 2, Case 3, and Case 4, we see that reconstructed-image regularizations improve the unmixing performance.
- The results of experiments in Case 5 and Case 6 verify

TABLE VI
THE SRE, RMSE, Ps, MPSNR, AND MSSIM RESULTS IN THE EXPERIMENTS WITH THE REAL HS IMAGE.

Noise	Evaluation Target	Measures	Methods						
			CLSunSAL [14]	JSTV [15]	RSSUn-TV [18]	LGSU [21]	RCHU (HTV)	RCHU (SSTV)	RCHU (HSSTV)
Case 1	Abundance	SRE	12.04	11.58	10.99	19.21	12.51	11.74	11.80
		RMSE	0.1076	0.1134	0.1213	0.0469	0.1019	0.1113	0.1106
		Ps	0.39	0.37	0.36	0.45	0.40	0.39	0.39
	Reconstructed HS image	PSNR	37.78	37.15	37.02	38.19	38.26	37.94	37.99
Case 2	Abundance	SSIM	0.9873	0.9840	0.9835	0.9863	0.9900	0.9891	0.9898
		SRE	8.28	7.38	7.14	10.89	10.55	10.11	10.17
		RMSE	0.1658	0.1838	0.1889	0.1190	0.1277	0.1343	0.1333
		Ps	0.34	0.32	0.31	0.38	0.35	0.34	0.35
Case 3	Abundance	PSNR	32.25	31.53	31.47	32.08	33.35	33.16	33.50
		SSIM	0.9574	0.9459	0.9453	0.9495	0.9678	0.9659	0.9697
		SRE	4.79	9.85	2.89	3.78	12.45	11.77	11.84
		RMSE	0.2476	0.1383	0.3082	0.2924	0.1026	0.1109	0.1100
Case 4	Abundance	Ps	0.25	0.35	0.26	0.27	0.40	0.39	0.39
		PSNR	21.45	35.12	21.06	21.09	36.69	36.46	36.63
		SSIM	0.7990	0.9745	0.7647	0.7655	0.9846	0.9836	0.9849
	Reconstructed HS image	SRE	6.34	10.52	4.93	6.43	12.16	11.44	11.50
Case 5	Abundance	RMSE	0.2071	0.1281	0.2438	0.2046	0.1061	0.1152	0.1144
		Ps	0.31	0.36	0.29	0.33	0.39	0.38	0.39
		PSNR	26.04	36.00	25.55	25.68	37.37	37.08	37.16
	Reconstructed HS image	SSIM	0.8835	0.9793	0.8612	0.8636	0.9876	0.9865	0.9875
Case 6	Abundance	SRE	6.21	8.20	4.77	5.56	10.07	9.54	9.60
		RMSE	0.2102	0.1673	0.2482	0.2218	0.1348	0.1433	0.1424
		Ps	0.30	0.33	0.29	0.31	0.35	0.34	0.35
	Reconstructed HS image	PSNR	25.77	33.01	25.31	25.41	35.37	35.04	35.46
Case 7	Abundance	SSIM	0.8778	0.9624	0.8541	0.8558	0.9816	0.9797	0.9826
		SRE	5.59	5.85	4.01	4.61	7.23	6.90	6.96
		RMSE	0.2258	0.2192	0.2711	0.2502	0.1871	0.1943	0.1929
		Ps	0.28	0.29	0.27	0.28	0.31	0.31	0.31
Case 8	Reconstructed HS image	PSNR	25.04	29.26	24.51	24.59	31.70	31.29	31.70
		SSIM	0.8564	0.9167	0.8290	0.8304	0.9599	0.9540	0.9614

that RCHU accurately estimates abundance maps if HS images are degraded by various types of noise.

- RCHU achieves good unmixing performance in experiments on both synthetic and real HS images.

VI. CONCLUSION

In this paper, we have proposed a new method for noise-robust unmixing. RCHU adopts the reconstructed-image regularization and explicitly handles three types of noises. We have formulated the unmixing problem as a constrained convex optimization problem that includes the regularization, and have developed the optimization algorithm based on P-PDS. Experiments on synthetic and real HS images have demonstrated the superiority of RCHU over existing methods. RCHU will have strong impacts on the field of remote sensing, including the estimation of abundance maps from HS images taken in measurement environments with severe degradation. For future work, we achieve more noise-robust blind unmixing by incorporating RCHU into learning-based methods.

REFERENCES

- [1] P. Ghamisi, N. Yokoya, J. Li, W. Liao, S. Liu, J. Plaza, B. Rasti, and A. Plaza, "Advances in hyperspectral image and signal processing: A comprehensive overview of the state of the art," *IEEE Geosci. Remote Sens. Mag.*, vol. 5, no. 4, pp. 37–78, 2017.
- [2] C.-I. Chang, *Hyperspectral imaging: techniques for spectral detection and classification*. Springer Science & Business Media, 2003, vol. 1.
- [3] P. S. Thenkabail and J. G. Lyon, *Hyperspectral remote sensing of vegetation*. CRC press, 2016.
- [4] B. Lu, P. D. Dao, J. Liu, Y. He, and J. Shang, "Recent advances of hyperspectral imaging technology and applications in agriculture," *Remote Sens.*, vol. 12, no. 16, p. 2659, 2020.
- [5] N. Keshava and J. F. Mustard, "Spectral unmixing," *IEEE Signal Process. Mag.*, vol. 19, no. 1, pp. 44–57, 2002.
- [6] J. M. Bioucas-Dias, A. Plaza, N. Dobigeon, M. Parente, Q. Du, P. Gader, and J. Chanussot, "Hyperspectral unmixing overview: Geometrical, statistical, and sparse regression-based approaches," *IEEE J. Sel. Top. Appl. Earth. Obs. Remote Sens.*, vol. 5, no. 2, pp. 354–379, 2012.
- [7] W. Ma, J. M. Bioucas-Dias, T. Chan, N. Gillis, P. Gader, A. Plaza, A. Ambikapathi, and C. Chi, "A signal processing perspective on hyperspectral unmixing: Insights from remote sensing," *IEEE Signal Process. Mag.*, vol. 31, no. 1, pp. 67–81, Jan. 2014.
- [8] B. Rasti, P. Scheunders, P. Ghamisi, G. Licciardi, and J. Chanussot, "Noise reduction in hyperspectral imagery: Overview and application," *Remote Sensing*, vol. 10, no. 3, p. 482, 2018.
- [9] Y. Zhao and J. Yang, "Hyperspectral image denoising via sparse representation and low-rank constraint," *IEEE Trans. Geosci. Remote Sens.*, vol. 53, no. 1, pp. 296–308, 2014.
- [10] G. Licciardi, F. Pacifici, D. Tuia, Prasad, T. West, F. Giacco, and et al., "Decision fusion for the classification of hyperspectral data: Outcome of the 2008 grs-s data fusion contest," *IEEE Trans. Geosci. Remote Sens.*, vol. 47, no. 11, pp. 3857–3865, 2009.

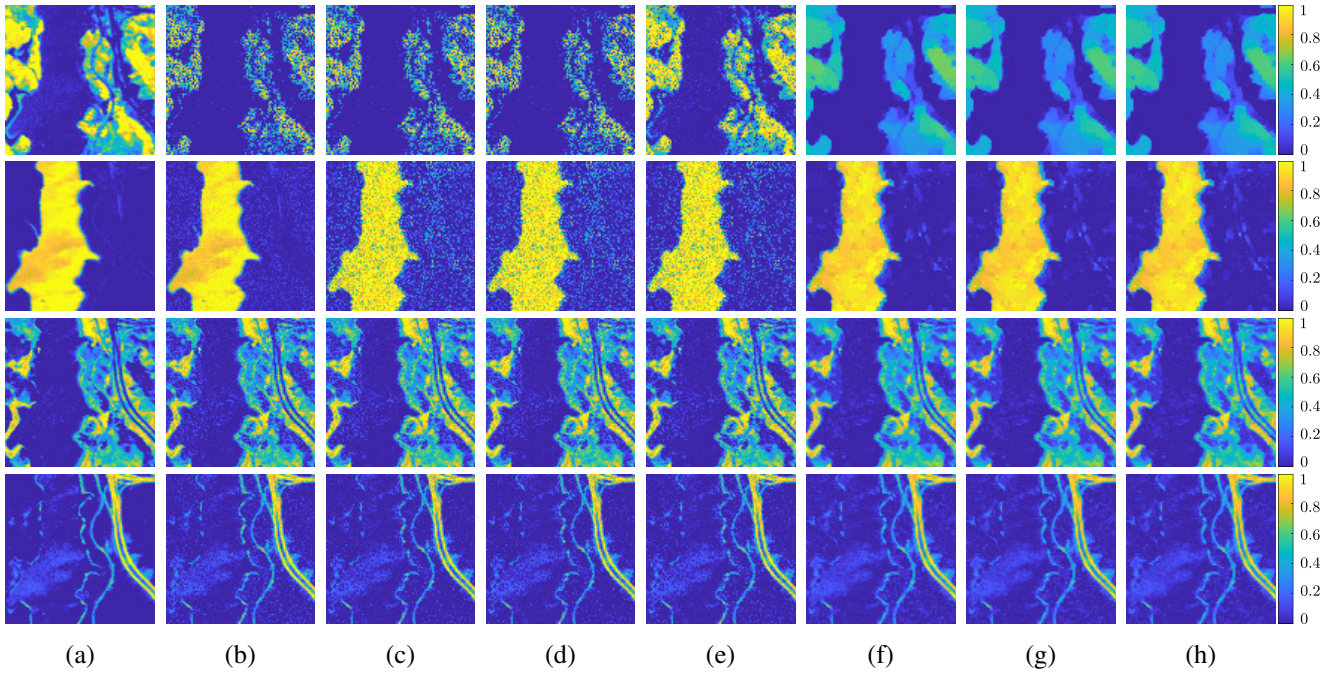


Fig. 10. Unmixing results of abundance maps for the real data in Case 2. (a): Original abundance maps. (b): CLSUnSAL [14]. (c): JSTV [15]. (d): RSSUn-TV [18]. (e): LGSU [21]. (f): **RCHU (HTV)**. (g): **RCHU (SSTV)**. (h): **RCHU (HSSTV)**.

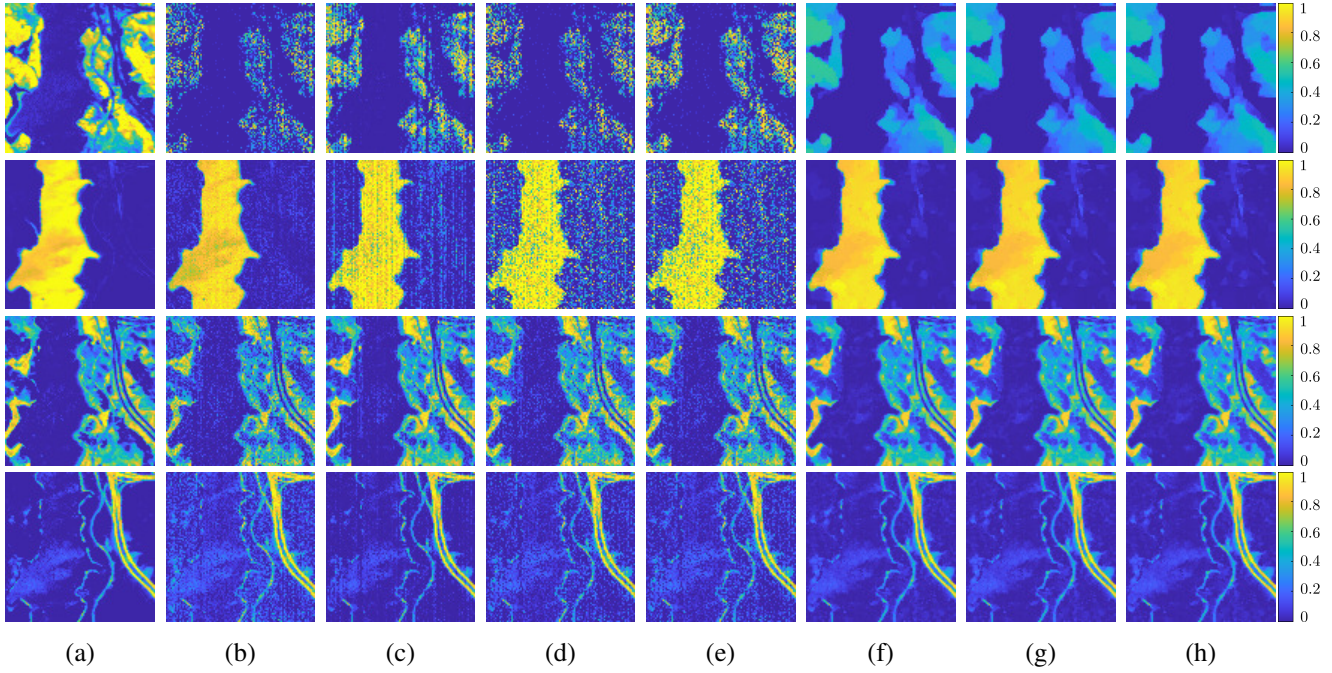


Fig. 11. Unmixing results of abundance maps for the real data in Case 5. (a): Original abundance maps. (b): CLSUnSAL [14]. (c): JSTV [15]. (d): RSSUn-TV [18]. (e): LGSU [21]. (f): **RCHU (HTV)**. (g): **RCHU (SSTV)**. (h): **RCHU (HSSTV)**.

- [11] N. Yokoya, C. Grohnfeldt, and J. Chanussot, "Hyperspectral and multispectral data fusion: A comparative review of the recent literature," *IEEE Trans. Geosci. Remote Sens. Mag.*, vol. 5, no. 2, pp. 29–56, 2017.
- [12] M.-D. Iordache, J. M. Bioucas-Dias, and A. Plaza, "Sparse unmixing of hyperspectral data," *IEEE Trans. Geosci. Remote Sens.*, vol. 49, no. 6, pp. 2014–2039, 2011.
- [13] M.-D. Iordache, J. Bioucas-Dias, and A. Plaza, "Total variation spatial regularization for sparse hyperspectral unmixing," *IEEE Trans. Geosci. Remote Sens.*, vol. 50, no. 11, pp. 4484–4502, 2012.
- [14] M.-D. Iordache, J. M. Bioucas-Dias, and A. Plaza, "Collaborative sparse regression for hyperspectral unmixing," *IEEE Trans. Geosci. Remote Sens.*, vol. 52, no. 1, pp. 341–354, Jan. 2014.
- [15] H. K. Aggarwal and A. Majumdar, "Hyperspectral unmixing in the presence of mixed noise using joint-sparsity and total variation," *IEEE J. Sel. Top. Appl. Earth. Obs. Remote Sens.*, vol. 9, no. 9, pp. 4257–4266, 2016.
- [16] R. Wang, H. Li, A. Pizurica, J. Li, A. Plaza, and W. Emery, "Hyperspectral unmixing using double reweighted sparse regression and total variation," *IEEE Geosci. Remote Sens. Lett.*, vol. 14, no. 7, pp. 1146–1150, 2017.
- [17] S. Zhang, J. Li, C. Li, H. C. Deng, and A. Plaza, "Spectral-spatial weighted sparse regression for hyperspectral image unmixing," *IEEE*

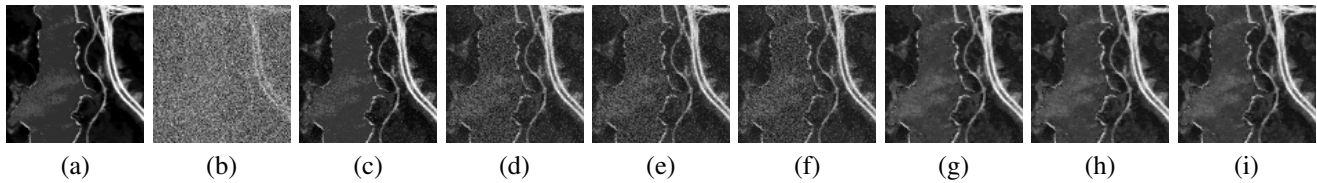


Fig. 12. Reconstructed HS image results for the real data in Case 2. (a): Original HS image. (b): Noisy image. (c): CLSUnSAL [14]. (d): JSTV [15]. (e): RSSUn-TV [18]. (f): LGSU [21]. (g): **RCHU (HTV)**. (h): **RCHU (SSTV)**. (i): **RCHU (HSSTV)**.

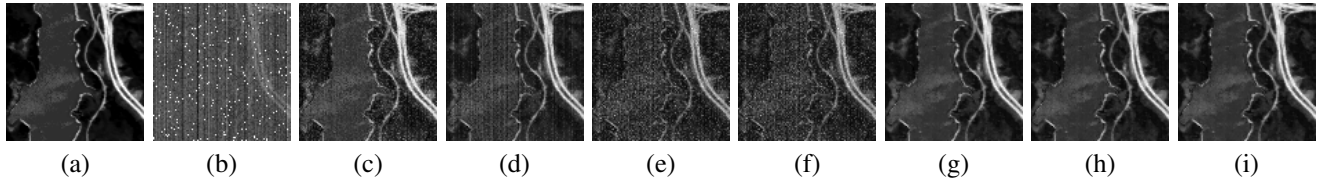


Fig. 13. Reconstructed HS image results for the real data in Case 5. (a): Original HS image. (b): Noisy image. (c): CLSUnSAL [14]. (d): JSTV [15]. (e): RSSUn-TV [18]. (f): LGSU [21]. (g): **RCHU (HTV)**. (h): **RCHU (SSTV)**. (i): **RCHU (HSSTV)**.

- Trans. Geosci. Remote Sens.*, vol. 56, no. 6, pp. 3265–3276, 2018.
- [18] J. Wang, T. Huang, J. Huang, H. Dou, L. Deng, and X. Zhao, “Row-sparsity spectral unmixing via total variation,” *IEEE J. Sel. Top. Appl. Earth. Obs. Remote Sens.*, vol. 12, no. 12, pp. 5009–5022, 2019.
- [19] H. Li, R. Feng, L. Wang, Y. Zhong, and L. Zhang, “Superpixel-based reweighted low-rank and total variation sparse unmixing for hyperspectral remote sensing imagery,” *IEEE Trans. Geosci. Remote Sens.*, vol. 59, no. 1, pp. 629–647, 2020.
- [20] L. Ren, Z. Ma, F. Bovolo, and L. Bruzzone, “A nonconvex framework for sparse unmixing incorporating the group structure of the spectral library,” *IEEE Trans. Geosci. Remote Sens.*, vol. 60, pp. 1–19, 2021.
- [21] X. Shen, H. Liu, X. Zhang, K. Qin, and X. Zhou, “Superpixel-guided local sparsity prior for hyperspectral sparse regression unmixing,” *IEEE Geosci. Remote Sens. Lett.*, vol. 19, pp. 1–5, 2022.
- [22] S. Ozkan, B. Kaya, and B. Akar, G, “Endnet: Sparse autoencoder network for endmember extraction and hyperspectral unmixing,” *IEEE Trans. Geosci. Remote Sens.*, vol. 57, no. 1, pp. 482–496, 2018.
- [23] B. Rasti, B. Koirala, P. Scheunders, and J. Chanussot, “MiSiCNet: Minimum simplex convolutional network for deep hyperspectral unmixing,” *IEEE Trans. Geosci. Remote Sens.*, vol. 60, pp. 1–15, Jan. 2022.
- [24] D. Hong, L. Gao, J. Yao, N. Yokoya, J. Chanussot, U. Heiden, and B. Zhang, “Endmember-guided unmixing network (EGU-Net): A general deep learning framework for self-supervised hyperspectral unmixing,” *IEEE Trans. Neural Netw. Learn. Syst.*, vol. 33, no. 11, pp. 6518–6531, Nov. 2022.
- [25] R. Heylen, M. Parente, and P. Gader, “A review of nonlinear hyperspectral unmixing methods,” *IEEE J. Sel. Top. Appl. Earth. Obs. Remote Sens.*, vol. 7, no. 6, pp. 1844–1868, 2014.
- [26] J. Huang, T. Huang, L. Deng, and X. Zhao, “Joint-sparse-blocks and low-rank representation for hyperspectral unmixing,” *IEEE Trans. Geosci. Remote Sens.*, vol. 57, no. 4, pp. 2419–2438, 2018.
- [27] H. Carfantan and J. Idier, “Statistical linear destriping of satellite-based pushbroom-type images,” *IEEE Trans. Geosci. Remote Sens.*, vol. 48, no. 4, pp. 1860–1871, Feb. 2010.
- [28] X. Liu, H. Shen, Q. Yuan, X. Lu, and C. Zhou, “A universal destriping framework combining 1-d and 2-d variational optimization methods,” *IEEE Trans. Geosci. Remote Sens.*, vol. 56, no. 2, pp. 808–822, Feb. 2018.
- [29] K. Naganuma and S. Ono, “A general destriping framework for remote sensing images using flatness constraint,” *IEEE Trans. Geosci. Remote Sens.*, vol. 60, pp. 1–16, Feb. 2022.
- [30] Q. Yuan, L. Zhang, and H. Shen, “Hyperspectral image denoising employing a spectral-spatial adaptive total variation model,” *IEEE Trans. Geosci. Remote Sens.*, vol. 50, no. 10, pp. 3660–3677, 2012.
- [31] W. Zhang, H. He, L. Zhang, H. Shen, and Q. Yuan, “Hyperspectral image restoration using low-rank matrix recovery,” *IEEE Trans. Geosci. Remote Sens.*, vol. 52, no. 8, pp. 4729–4743, 2013.
- [32] W. He, H. Zhang, L. Zhang, and H. Shen, “Total-variation-regularized low-rank matrix factorization for hyperspectral image restoration,” *IEEE Trans. Geosci. Remote Sens.*, vol. 54, no. 1, pp. 178–188, 2015.
- [33] H. K. Aggarwal and A. Majumdar, “Hyperspectral image denoising using spatio-spectral total variation,” *IEEE Geosci. Remote Sens. Lett.*, vol. 13, no. 3, pp. 442–446, 2016.
- [34] S. Takeyama, S. Ono, and I. Kumazawa, “A constrained convex optimization approach to hyperspectral image restoration with hybrid spatio-spectral regularization,” *Remote Sens.*, vol. 12, no. 21, p. 3541, 2020.
- [35] M. Wang, Q. Wang, J. Chanussot, and D. Hong, “ l_0 - l_1 hybrid total variation regularization and its applications on hyperspectral image mixed noise removal and compressed sensing,” *IEEE Trans. Geosci. Remote Sens.*, vol. 59, no. 9, pp. 7695–7710, 2021.
- [36] S. Takemoto, K. Naganuma, and S. Ono, “Graph spatio-spectral total variation model for hyperspectral image denoising,” *IEEE Geosci. Remote Sens. Lett.*, vol. 19, pp. 1–5, Jul. 2022.
- [37] T. Pock and A. Chambolle, “Diagonal preconditioning for first order primal-dual algorithms in convex optimization,” in *2011 International Conference on Computer Vision*. IEEE, 2011, pp. 1762–1769.
- [38] K. Naganuma and S. Ono, “Operator-norm-based variable-wise diagonal preconditioning for automatic stepsize selection of a primal-dual splitting algorithm,” in *Proc. Eur. Signal Process. Conf. (EUSIPCO)*, Aug. 2022.
- [39] K. Naganuma and S. Ono, “Variable-wise diagonal preconditioning for primal-dual splitting: Design and applications,” *arXiv:2301.08468*, 2023. [Online]. Available: <https://arxiv.org/abs/2301.08468>
- [40] A. Chambolle and T. Pock, “A first-order primal-dual algorithm for convex problems with applications to imaging,” *J. Math. Imag. Vis.*, vol. 40, no. 1, pp. 120–145, 2011.
- [41] M. Afonso, J. Bioucas-Dias, and M. Figueiredo, “An augmented Lagrangian approach to the constrained optimization formulation of imaging inverse problems,” *IEEE Trans. Image Process.*, vol. 20, no. 3, pp. 681–695, 2011.
- [42] G. Chierchia, N. Pustelnik, J. Pesquet, and B. Pesquet-Popescu, “Epigraphical projection and proximal tools for solving constrained convex optimization problems,” *Signal, Image Video Process.*, vol. 9, no. 8, pp. 1737–1749, 2015.
- [43] S. Ono and I. Yamada, “Signal recovery with certain involved convex data-fidelity constraints,” *IEEE Trans. Signal Process.*, vol. 63, no. 22, pp. 6149–6163, Nov. 2015.
- [44] S. Ono, “Primal-dual plug-and-play image restoration,” *IEEE Signal Process. Lett.*, vol. 24, no. 8, pp. 1108–1112, Aug. 2017.
- [45] S. Ono, “Efficient constrained signal reconstruction by randomized epigraphical projection,” in *Proc. IEEE Int. Conf. Acoust., Speech Signal Process. (ICASSP)*. IEEE, 2019, pp. 4993–4997.
- [46] L. Condat, “Fast projection onto the simplex and the l_1 ball,” *Math. Program.*, vol. 158, no. 1, pp. 575–585, Jul. 2016.
- [47] C. Rodarmel and J. Shan, “Principal component analysis for hyperspectral image classification,” *Surv. Land Inf. Sci.*, vol. 62, no. 2, pp. 115–122, 2002.
- [48] Z. Wang, A. Bovik, H. Sheikh, and E. Simoncelli, “Image quality assessment: from error visibility to structural similarity,” *IEEE Trans. Image Process.*, vol. 13, no. 4, pp. 600–612, Apr. 2004.



Kazuki Naganuma (S'21) received a B.E. degree and M.E. degree in Information and Computer Sciences in 2020 from the Kanagawa Institute of Technology and from the Tokyo Institute of Technology, respectively.

He is currently pursuing an Ph.D. degree at the Department of Computer Science in the Tokyo Institute of Technology. His current research interests are in signal and image processing and optimization theory.

Mr. Naganuma received the Student Conference Paper Award from IEEE SPS Japan Chapter in 2023.



Yuki Nagamatsu received a B.E. degree in Information and Computer Sciences in 2021 from the Tokyo Institute of Technology.

She is currently pursuing an M.E. degree at the Department of Computer Science in the Tokyo Institute of Technology.



Shunsuke Ono (S'11–M'15) received a B.E. degree in Computer Science in 2010 and M.E. and Ph.D. degrees in Communications and Computer Engineering in 2012 and 2014 from the Tokyo Institute of Technology, respectively.

From April 2012 to September 2014, he was a Research Fellow (DC1) of the Japan Society for the Promotion of Science (JSPS). He is currently an Associate Professor in the Department of Computer Science, School of Computing, Tokyo Institute of Technology. From October 2016 to March 2020 and

from October 2021 to present, he was/is a Researcher of Precursory Research for Embryonic Science and Technology (PRESTO), Japan Science and Technology Corporation (JST), Tokyo, Japan. His research interests include signal processing, image analysis, remote sensing, mathematical optimization, and data science.

Dr. Ono received the Young Researchers' Award and the Excellent Paper Award from the IEICE in 2013 and 2014, respectively, the Outstanding Student Journal Paper Award and the Young Author Best Paper Award from the IEEE SPS Japan Chapter in 2014 and 2020, respectively, the Funai Research Award from the Funai Foundation in 2017, the Ando Incentive Prize from the Foundation of Ando Laboratory in 2021, and the Young Scientists' Award from MEXT in 2022. He has been an Associate Editor of IEEE TRANSACTIONS ON SIGNAL AND INFORMATION PROCESSING OVER NETWORKS since 2019.